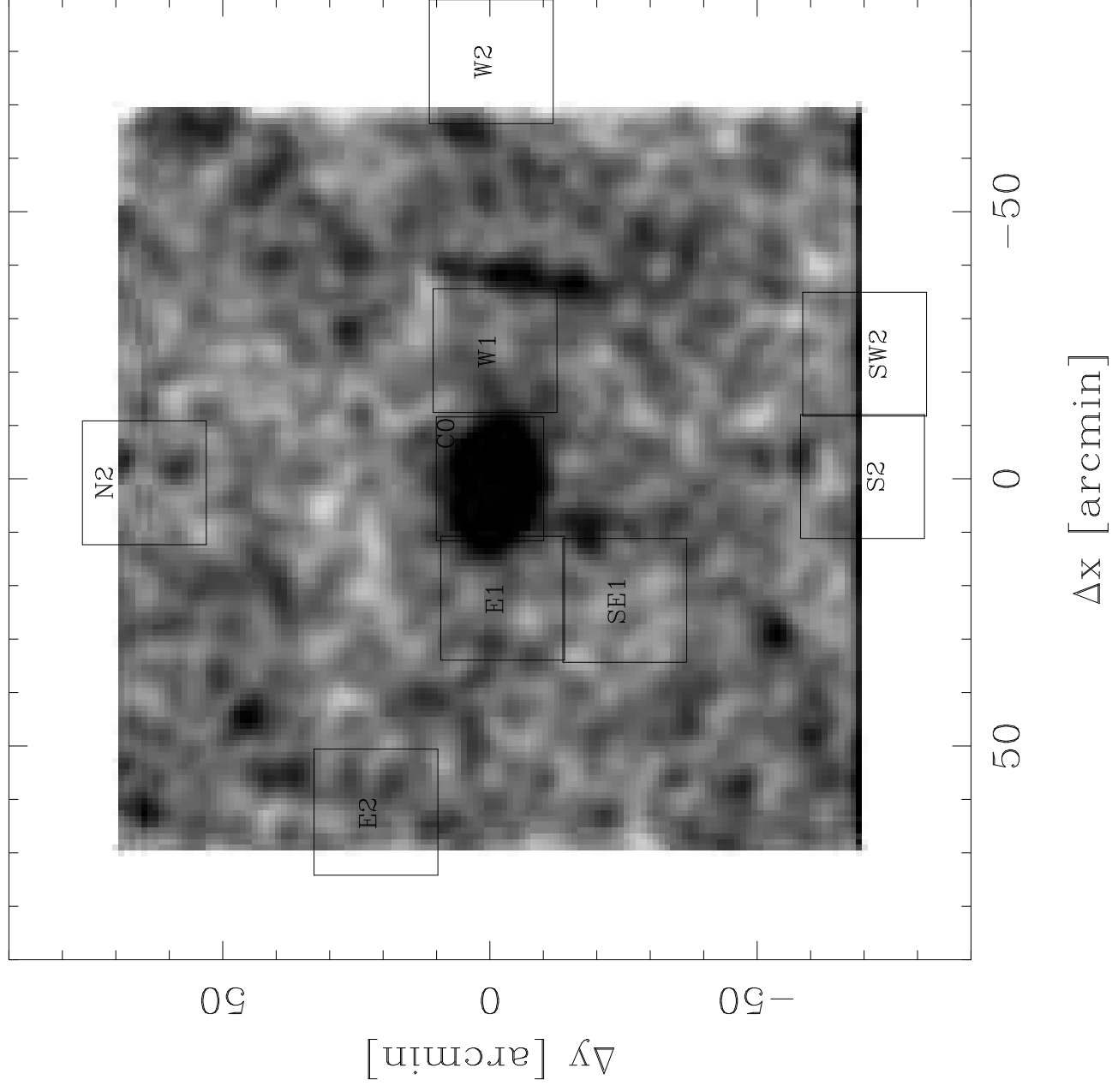
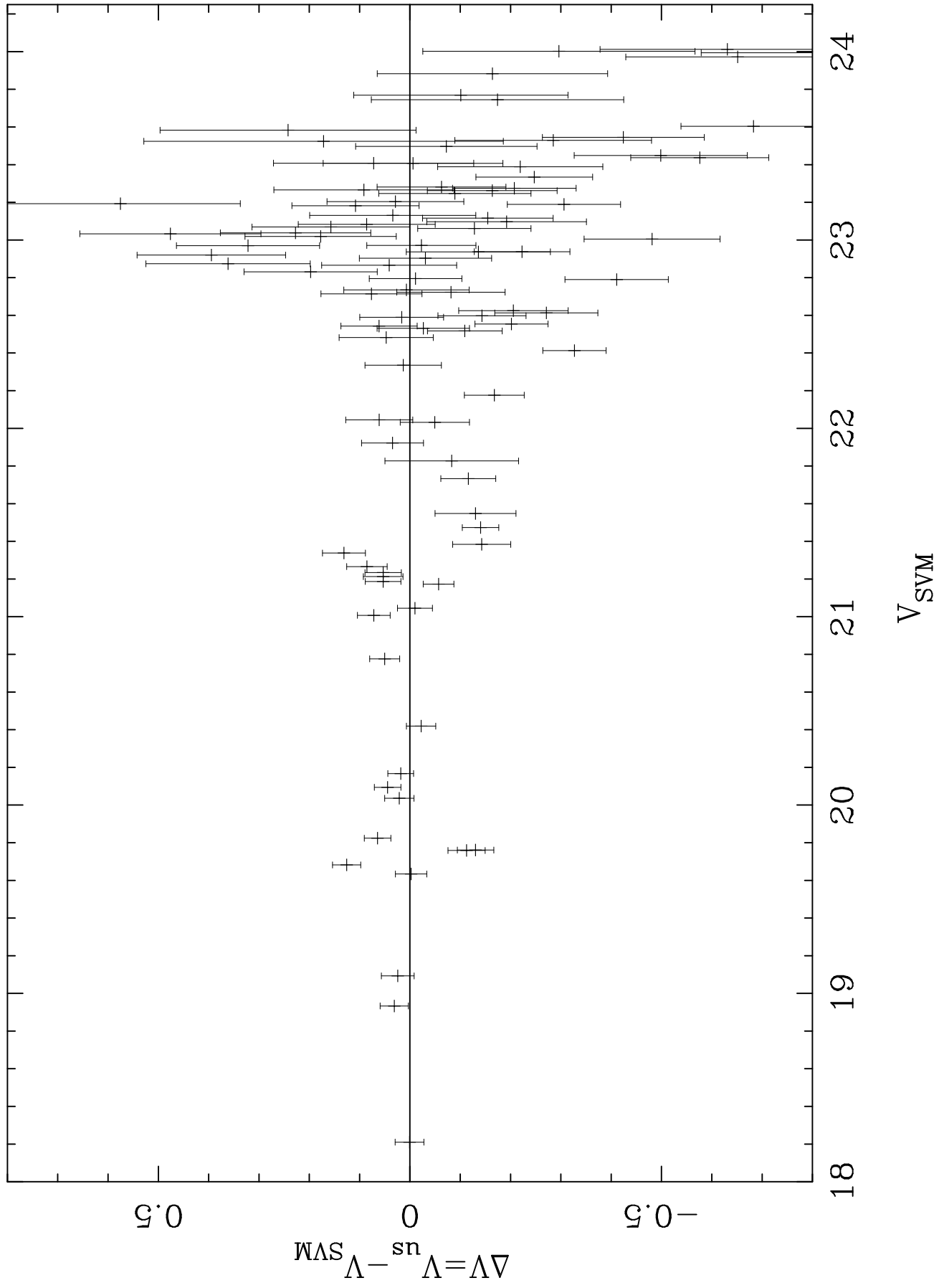
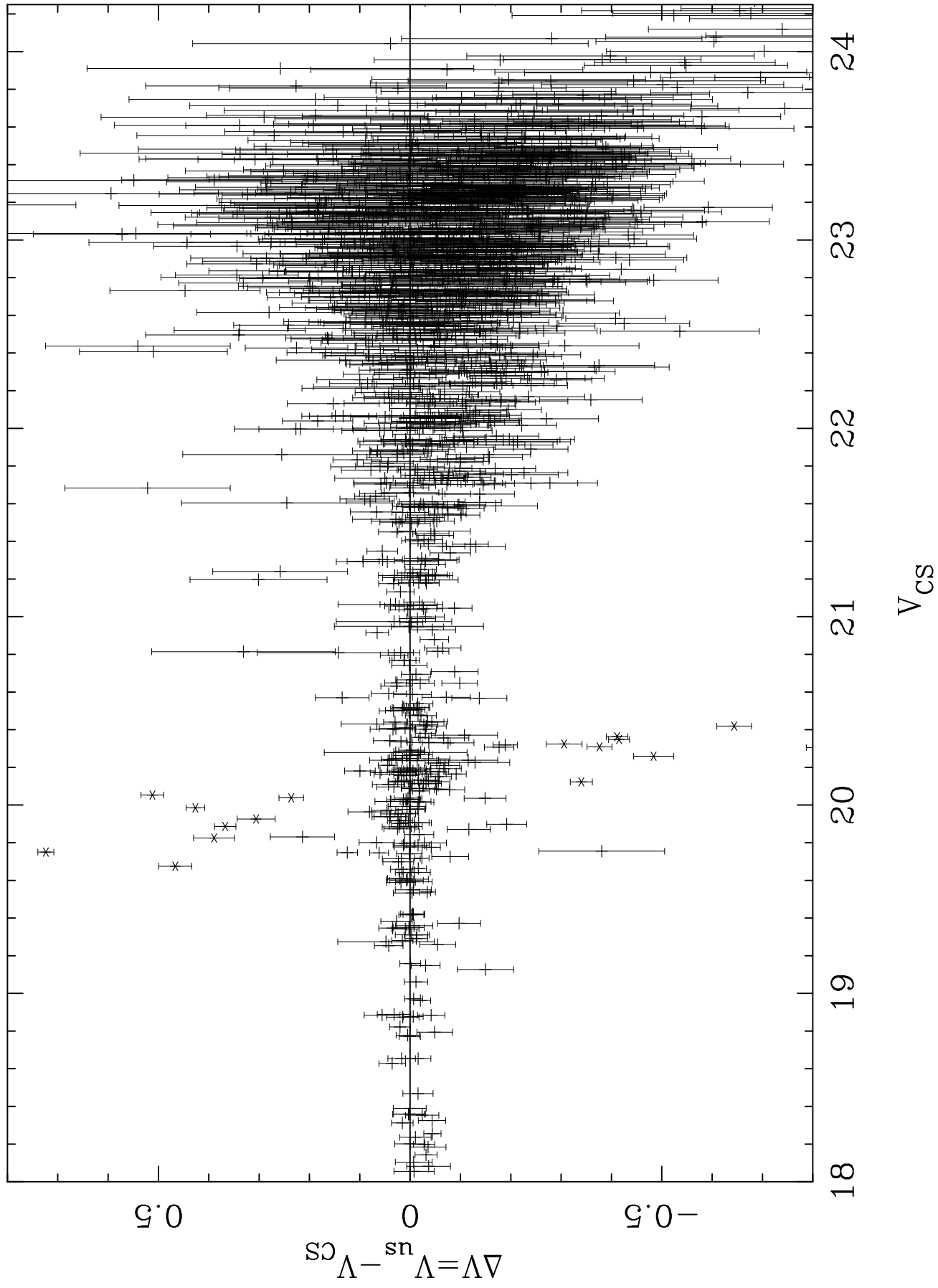


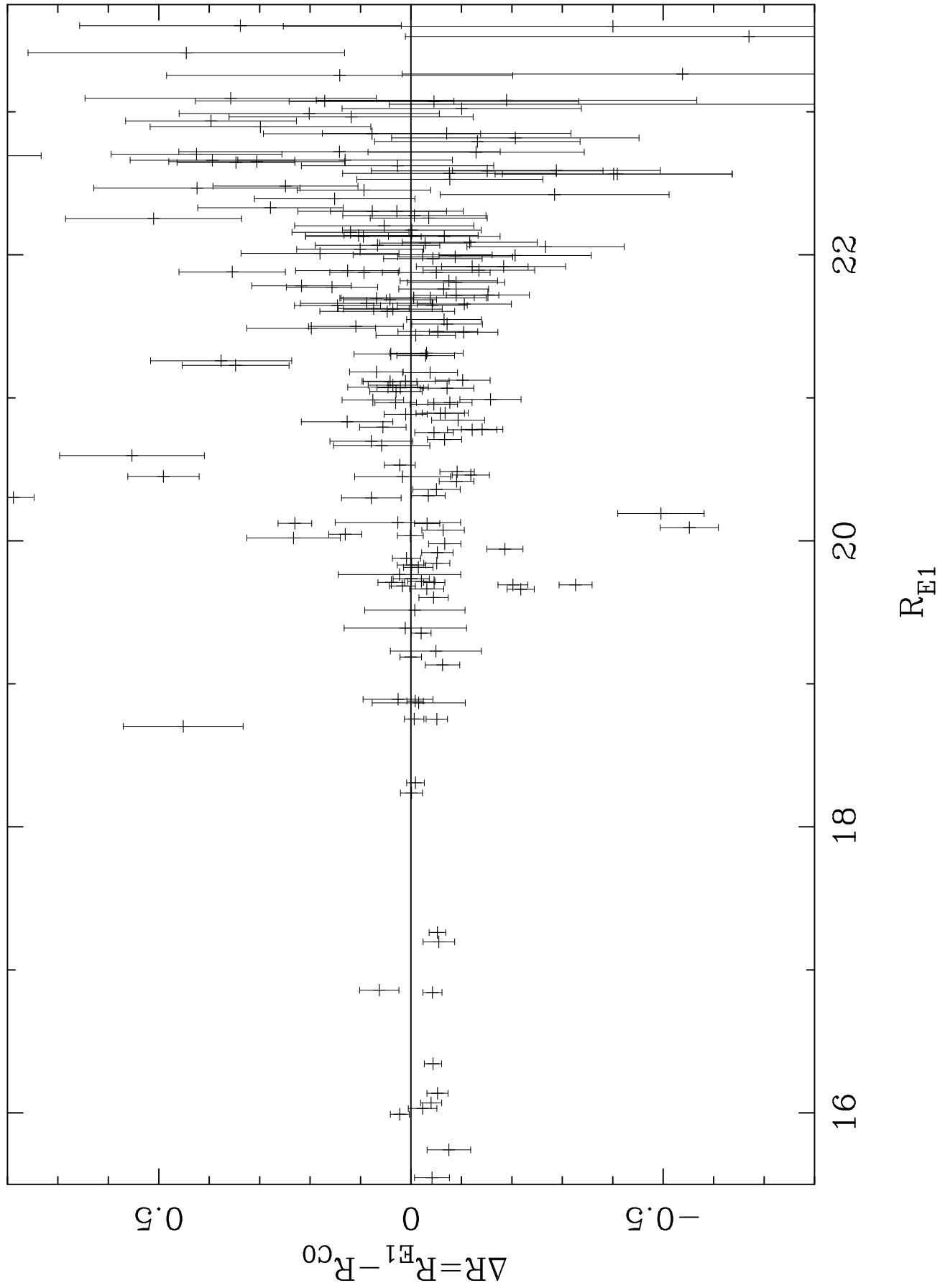
This figure "piatek.fig1.jpg" is available in "jpg" format from:

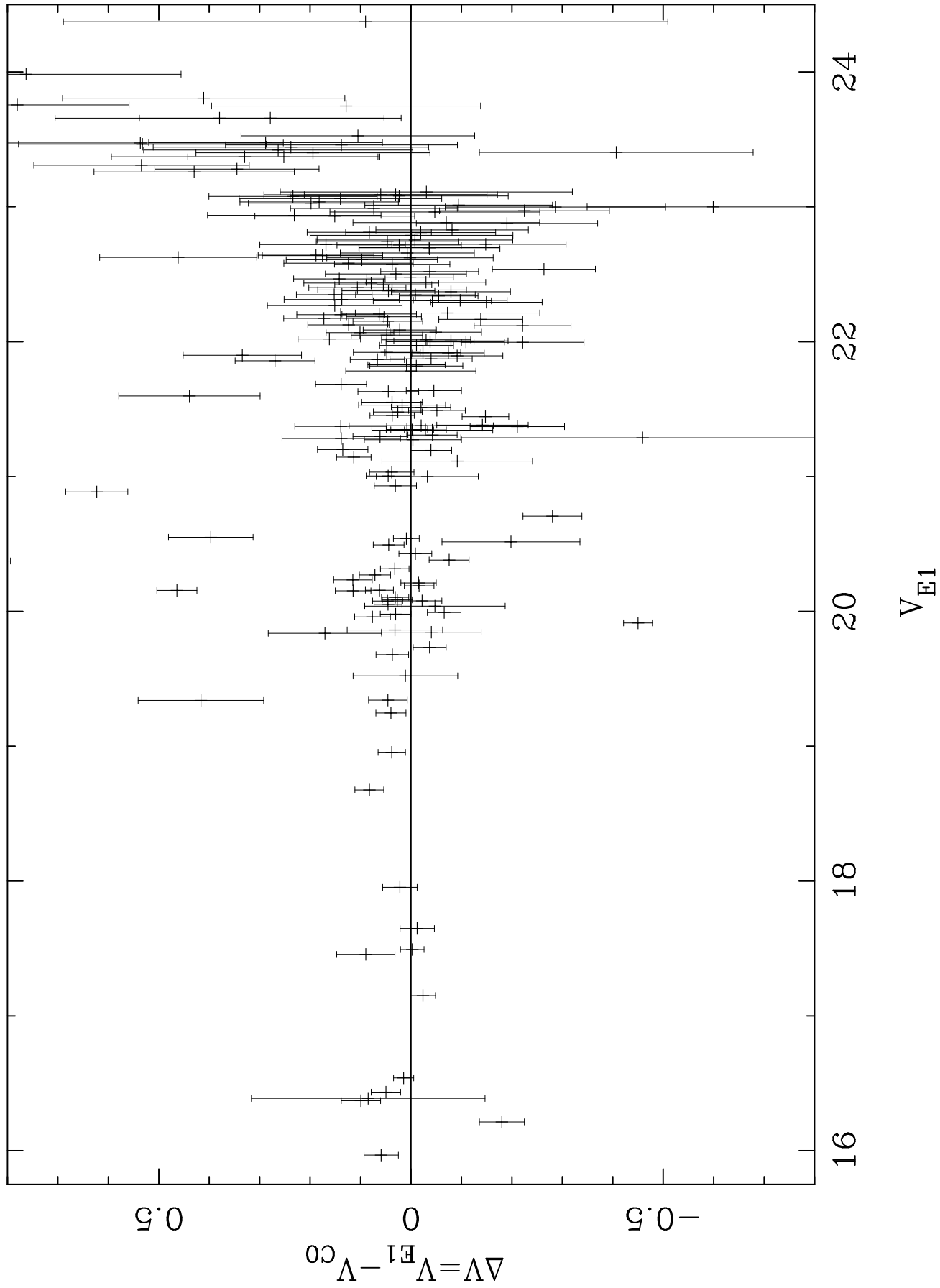
<http://arxiv.org/ps/astro-ph/0011006v1>

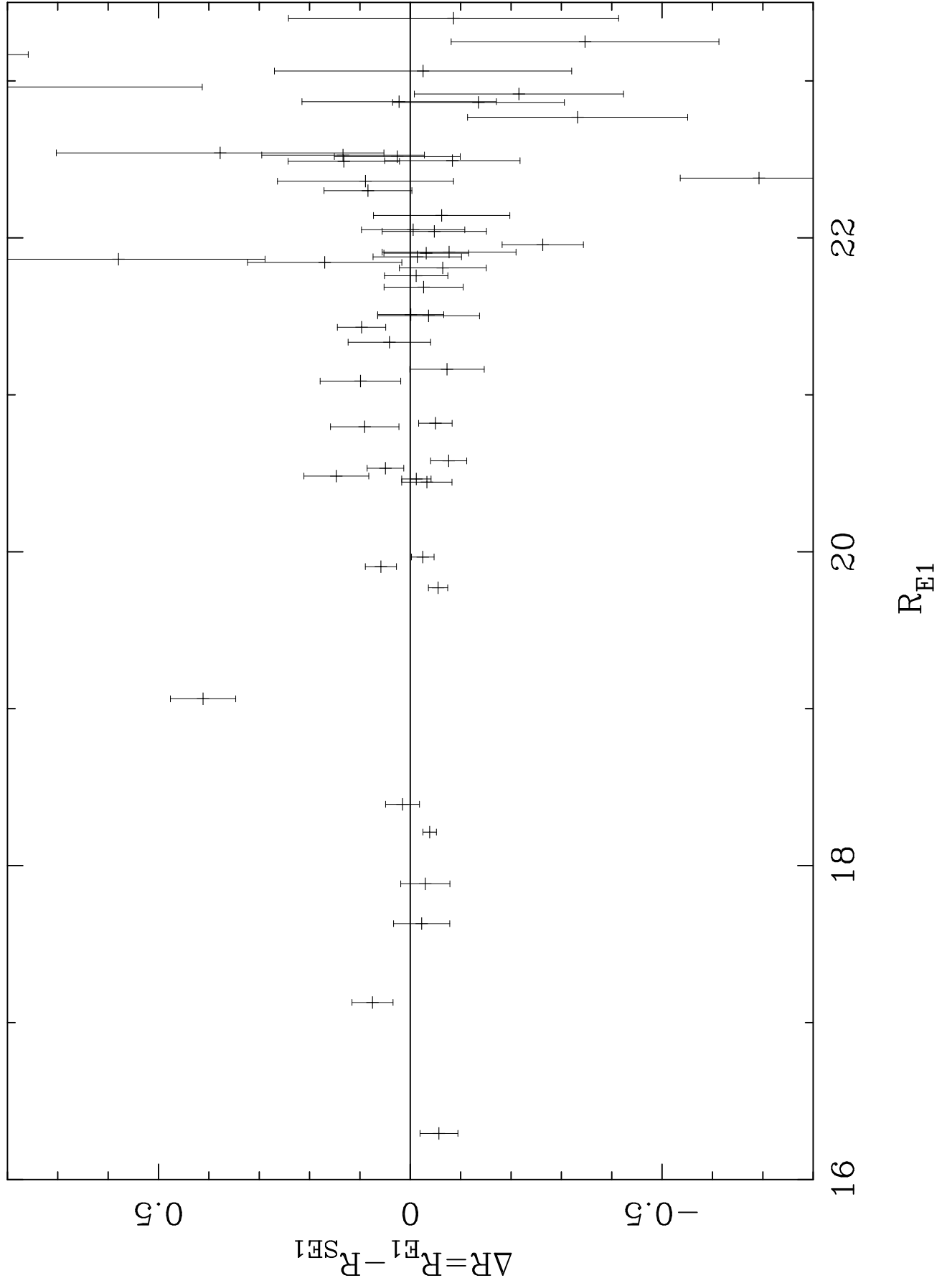


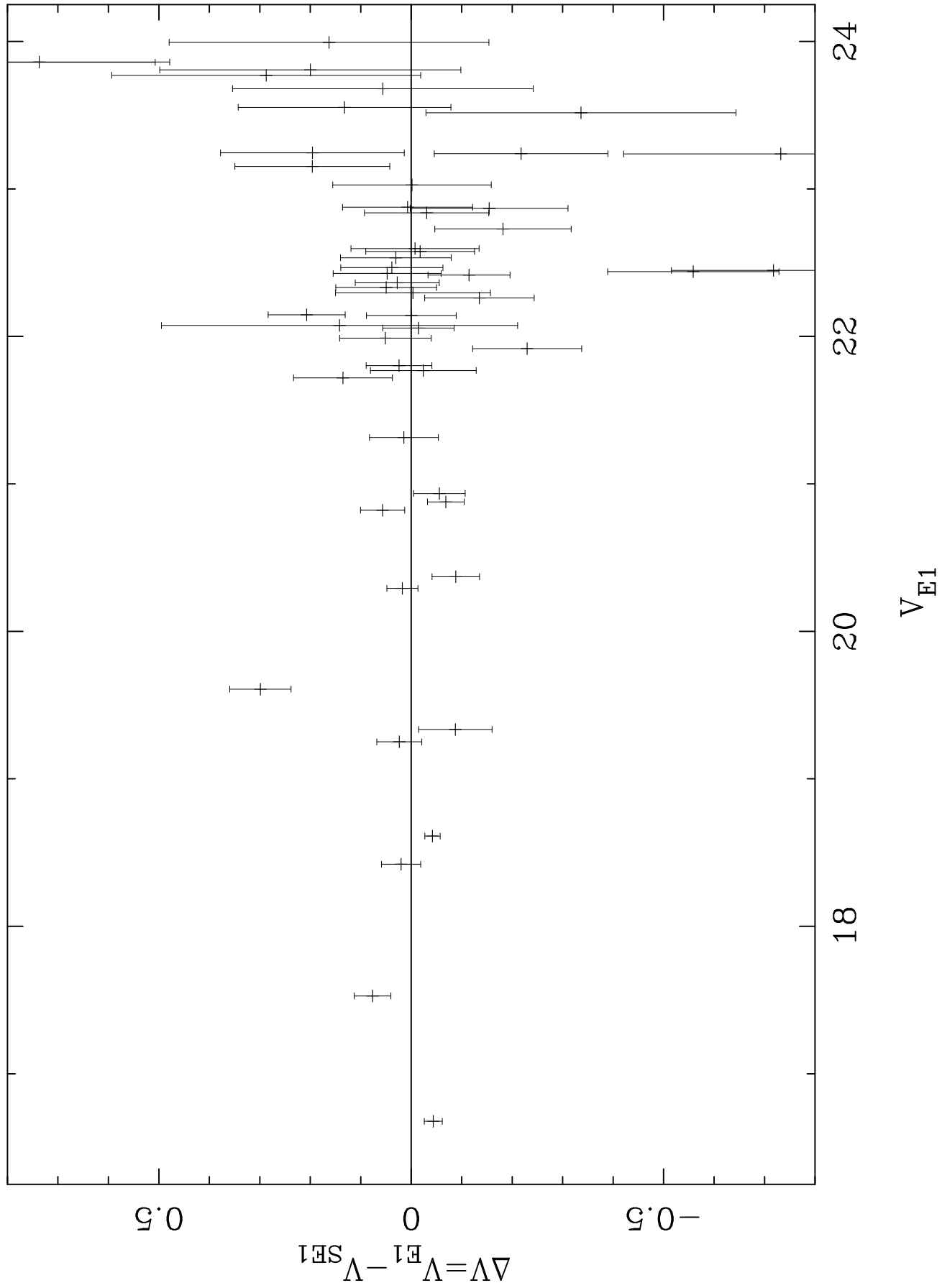


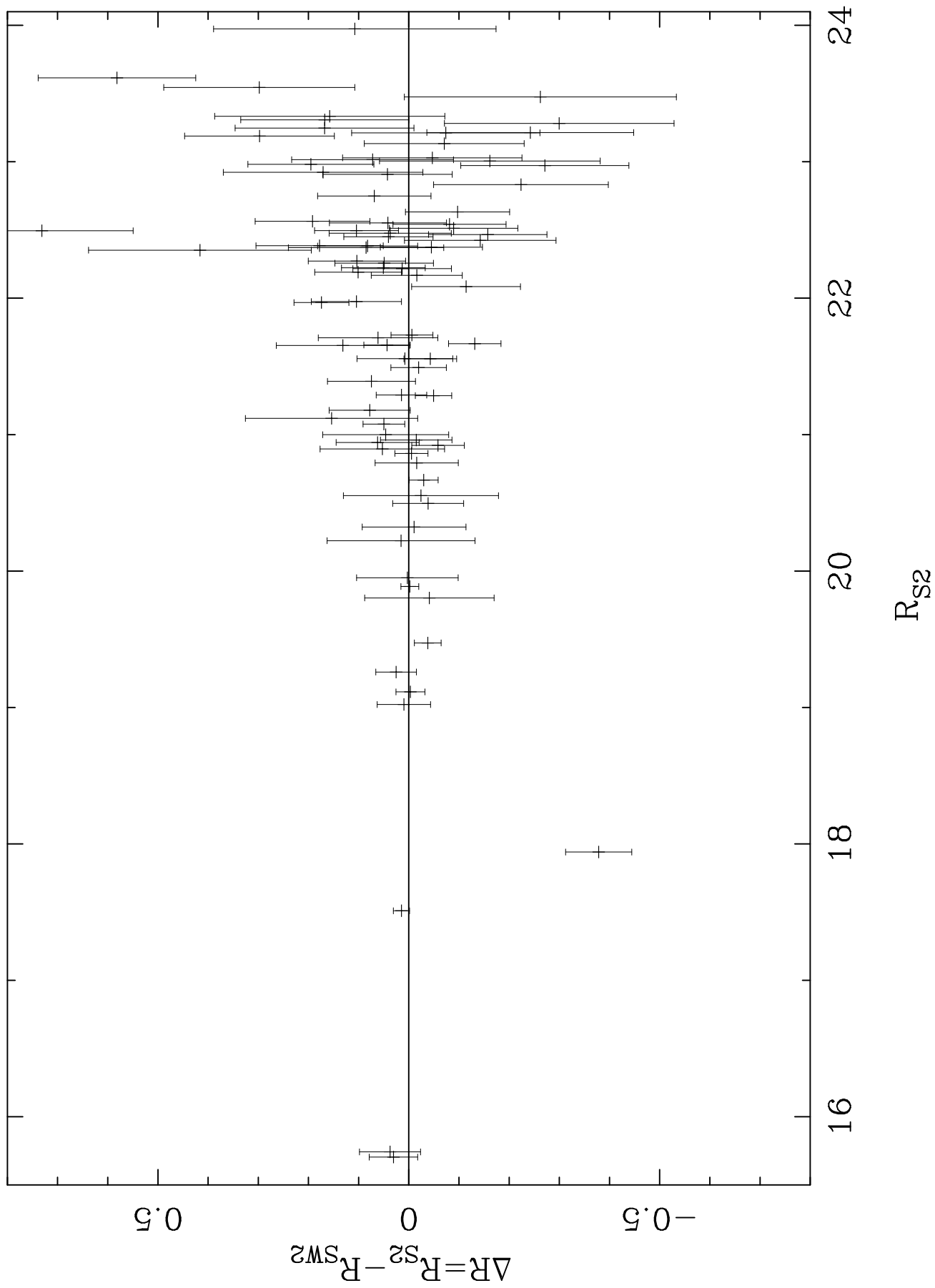


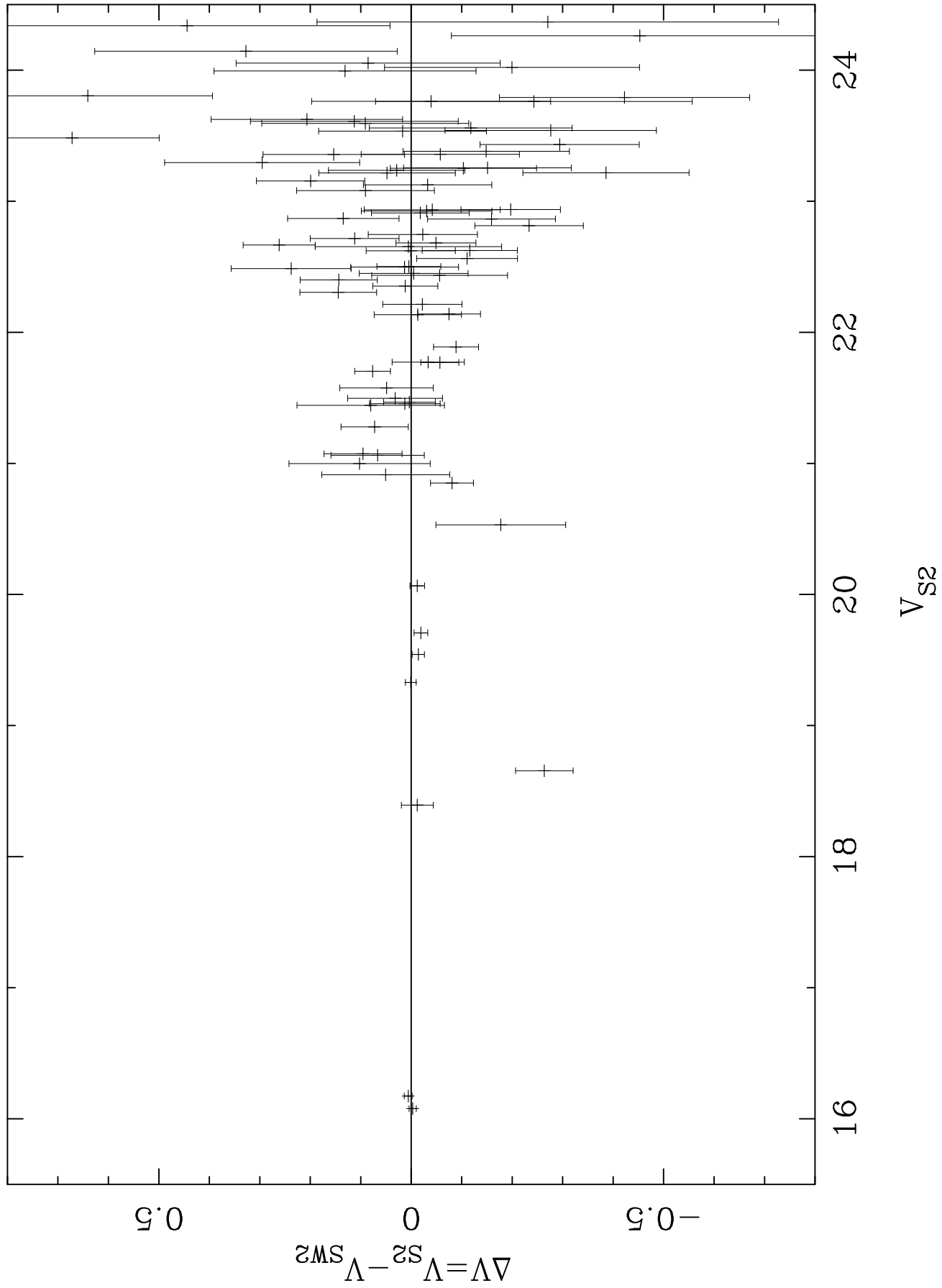


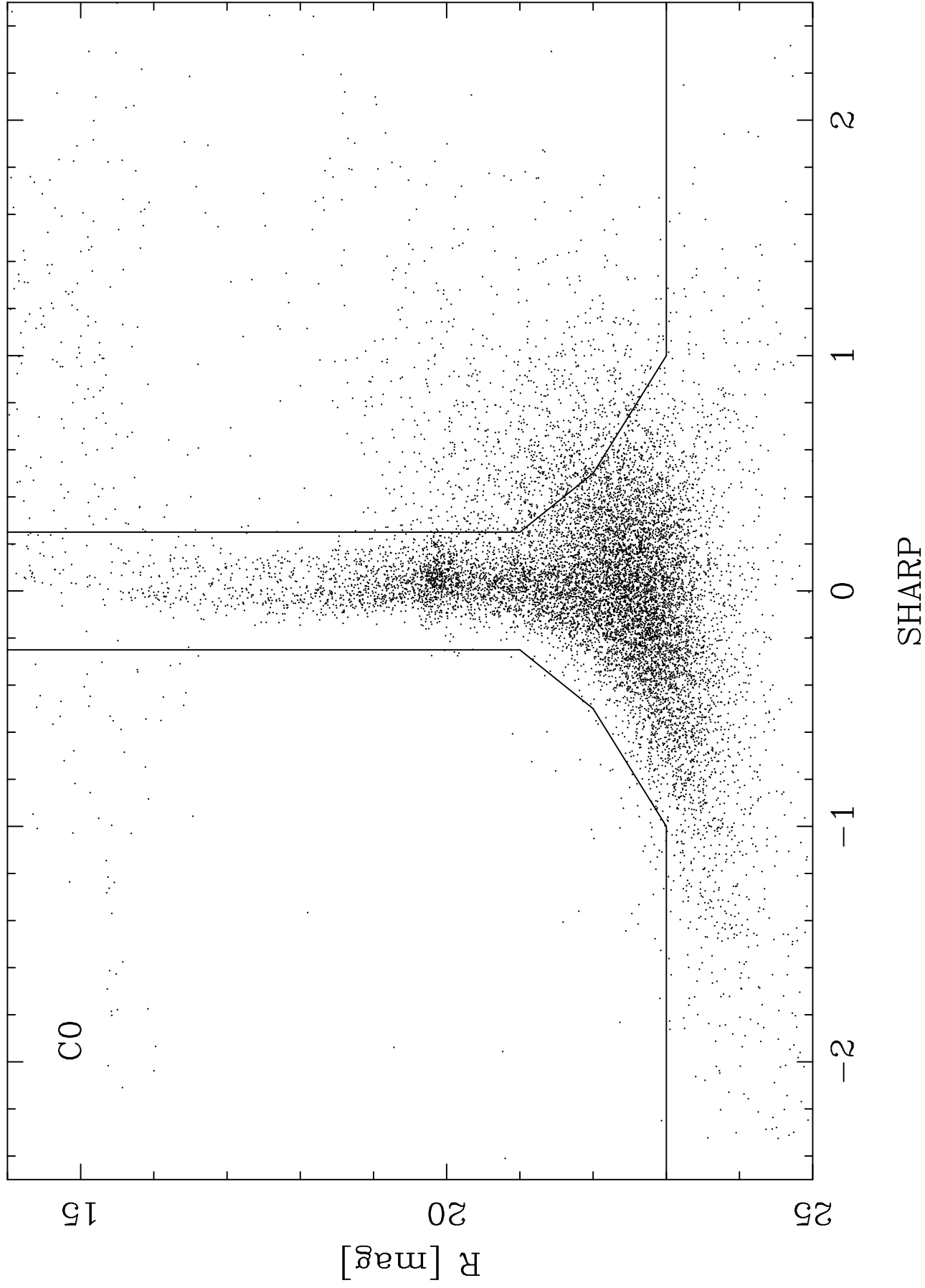












This figure "piatek.fig9.gif" is available in "gif" format from:

<http://arxiv.org/ps/astro-ph/0011006v1>

Stars of the Draco Dwarf Spheroidal Galaxy Beyond its Measured Tidal Boundary

Slawomir Piatek

Dept. of Physics, New Jersey Institute of Technology, Newark, NJ 07102

E-mail address: piatek@physics.rutgers.edu

Carlton Pryor¹

Dept. of Physics and Astronomy, Rutgers, the State University of New Jersey,
136 Frelinghuysen Rd., Piscataway, NJ 08854–8019

E-mail address: pryor@physics.rutgers.edu

Taft E. Armandroff

National Optical Astronomy Observatory, P.O. Box 26732, Tucson, AZ 85726

E-mail address: tarmandroff@noao.edu

and

Edward W. Olszewski¹

Steward Observatory, University of Arizona, Tucson, AZ 85721

Email address: eolszewski@as.arizona.edu

ABSTRACT

We report R - and V -band photometry derived from CCD imaging for objects in nine fields in and around the Draco dwarf spheroidal galaxy. The most distant fields are about 1.3° from the center. We use these data to search for Draco stars outside of its measured tidal boundary. The search involves three methods: 1) Plotting color-magnitude diagrams for individual fields, for sections of fields, and for combined fields and sections. A color-magnitude diagram can reveal a population of Draco stars by the presence of the expected principal sequences. 2) Measuring field-to-field fluctuations and 3) measuring intra-field fluctuations in the surface density of objects located near the Draco principal sequences in the color-magnitude diagram. We find evidence for the presence of Draco stars

¹Visiting Astronomer, Kitt Peak National Observatory, National Optical Astronomy Observatory, which is operated by the Association of Universities for Research in Astronomy, Inc. (AURA) under cooperative agreement with the National Science Foundation.

immediately beyond the measured tidal boundary of Draco and place an upper limit on the number of such stars in more distant fields that lie close to the extension of its major axis. The best evidence is the presence of the Draco principal sequences in the color-magnitude diagram for some combined fields and sections of fields. The measurements of the field-to-field fluctuations in the stellar surface density confirm this result.

Subject headings: galaxies: dwarf — galaxies: individual (Draco) — galaxies: stellar content — galaxies: structure — galaxies: Local Group

1. Introduction

It is a long-standing question whether the tidal forces of the Milky Way have played, and continue to play, a significant role in the formation and evolution of its companion dwarf spheroidal (dSph, hereafter) galaxies (e.g., Hodge & Michie 1969). Proposed effects of these forces on a dSph are episodic star formation (Lin & Murray 1998), a spuriously large measured mass-to-light ratio (e.g., Kuhn & Miller 1989; Bellazzini et al. 1996; Klessen & Kroupa 1998; but also see Pryor 1996; Olszewski 1998; Hirashita et al. 1999), and structural alterations of the outer regions. Examples of structural alterations are isophote twisting, truncation of the radial density profile, and the formation of extended streams of tidal debris. In this article we look for the last of these effects using star counts in two colors to search for stars of the Draco dSph beyond its measured tidal boundary.

Irwin & Hatzidimitriou (1995; hereafter IH) list the most accurately measured value of the “tidal radius” of Draco: 28.3 ± 2.4 arcmin along the major axis. They obtained this value by fitting a single-component King (1966) model to their projected density profile derived from star counts made using Palomar Schmidt plates digitized and analyzed using the APM facility (Kibblewhite et al. 1984). Because there is no fundamental reason why a King model must describe a dSph and, as IH note, the models do not fit the outer parts of their profiles well, this measured tidal radius should not be literally interpreted either as the limiting radius of a dSph or as the radius beyond which stars are unbound due to Galactic tides. Thus, this tidal radius should only be considered as a parameter in a fitted model. Throughout this article we use the phrase “tidal boundary” to mean the elliptical contour centered on Draco with a semi-major axis of 28.3 arcmin, an ellipticity of 0.29, and position angle of 82 degrees (IH). However, we do not automatically interpret Draco stars beyond this boundary as being unbound from Draco by Galactic tidal forces.

Even though the physical interpretation of the tidal radius resulting from fitting a King model to the projected density profile of a dSph is uncertain, the spatial structure of the outer regions of a dSph is an important source of information about the galaxy. The density profile of bound stars at large radii is needed to constrain the central density of dark matter in a dSph (Pryor 1994). Moore (1996) has emphasized that the radius beyond which most of the stars are unbound due to Galactic tidal forces constrains the total mass of a dSph and, hence, its total amount of dark matter. Johnston et al. (1999) identify this radius with that where the slope of the projected density profile in a log-log plot abruptly becomes shallower, based on numerical simulations of dSphs interacting with the tidal field of the Galaxy. The unbound stars also should show velocity gradients and a velocity dispersion increasing with increasing distance from the dSph (Oh et al. 1995; Piatek & Pryor 1995; Johnston et al. 1999). Observing these kinematic signatures is necessary to confirm that these stars are unbound from the dSph by Galactic tidal forces, since other mechanisms could produce an extended bound population with a shallow density profile at large radii. An example is a halo of stars that formed from gas pushed to large radii by supernovae and stellar winds.

In this article, we report R - and V -band photometry for objects in nine fields in and around Draco and the results of using these data to search for Draco stars beyond its measured tidal boundary. Section 2 describes the data acquisition and reduction. Section 3 presents color-magnitude diagrams for our fields and discusses the classification of an object based on its location in the diagram and the morphology of its image. Section 4 describes our methods of searching for Draco stars and the results they yield. Section 5 summarizes our results and compares them to the results from other similar studies.

2. Data Acquisition and Reduction

We imaged nine fields in and around Draco in the R and V bands using the KPNO 0.9-m telescope and two 2048×2048 pixel CCD chips: an engineering grade chip for the central field – reading out only 1747 columns – and the CCD designated T2KA for the rest. The image scale is 0.68 arcsec per pixel, yielding 23.2 arcmin square images for all but the central field. Table 1 contains the basic information about the fields. Column 1 lists their abbreviated names. Column 2 gives the date when each was imaged. Columns 3, 4, 5, and 6 list the equatorial and Galactic coordinates of the centers of the fields, respectively. Columns 7 and 8 list the combined exposure times in the V and R bands and the final two columns list the average full-width at half-maximum (FWHM), in pixels, measured for stellar images in the V and R frames. This value of the FWHM is an average of those for nine stars forming a rough 3×3 grid across a field and is followed by the root-mean-square (rms, hereafter)

scatter around the average. Generally, the seeing in the R band is better than that in the V band, that for the C0 and W2 fields being the exceptions. The scatter, indicative of intra-field focus variations, is generally small, except for the C0 and E1 fields. The smaller scatter for the other fields is due to a two-element corrector, installed between our 1993 and 1994 runs, which flattened the focal surface of the 0.9 m telescope (see Armandroff et al. 1993). Only in E1 are these variations large enough to cause problems with the photometry, which are discussed later in this section.

Figure 1 shows the configuration of the fields superimposed on a Digitized Sky Survey image centered on Draco. The ellipse depicts the measured tidal boundary of Draco; its semi-major axis and ellipticity are 28.3 arcmin and 0.29, respectively (IH). The tidal boundary encloses all of the C0 field, more than 50% of the E1 and W1 fields, and only about 10% of the SE1 field – the northwest corner. Figure 2 shows the fields superimposed on a map of the surface density of stars and galaxies derived by IH for a $2.3^\circ \times 2.3^\circ$ region centered on Draco. Figures 1 and 2 imply that fields C0, E1, W1, and SE1 contain Draco stars.

The data for each Draco field generally consists of four exposures in the V band and three in the R band (see columns 7 and 8 of Table 1 for details). We overscan subtracted, flattened, and trimmed each image in the usual way using IRAF². For the 1994 data, twilight flats produced the most uniform sky for the R images whereas dome flats produced the most uniform sky for the V images. For similar reasons, we used twilight flats for the 1993 (E1 field) V images and dome flats with an illumination correction based on the twilight sky for the R images. The 1991 C0 field had only dome flats available. Our next processing step was aligning and then combining the frames in a given band and field to form a single image. Our primary goal in combining frames was to eliminate contamination due to cosmic rays, satellites, meteors, etc.. The optimal rejection of deviant pixels requires consistent sky levels and stellar fluxes in the different frames. We multiplied each frame by the amount necessary to make the aperture fluxes of three bright, isolated stars equal, on average, to their fluxes averaged over all of the images. Additive corrections then made the average skies measured in the vicinity of these three stars equal. We averaged the frames using the IRAF IMCOMBINE subroutine using the “ccdclip” rejection algorithm with a 4σ rejection limit.

We used the stand-alone version of the photometry software package DAOPHOT (Stetson 1987, 1992, 1994) to find objects in the combined frames and to determine their magnitudes by fitting a point spread function (PSF, hereafter) derived from selected stars. About 100 stars determined the PSF on each averaged frame and the PSF varied quadratically with

²IRAF is distributed by the National Optical Astronomy Observatory, which is operated by the Association of Universities for Research in Astronomy, Inc., under contract to the National Science Foundation.

position within a frame. The DAOPHOT ALLSTAR program fits the PSF to each object found in the averaged frame, yielding the centroid, magnitude, uncertainty in the magnitude, sky level, CHI, and SHARP. The last two parameters measure how closely the fitted image matches the PSF. CHI is a robust measure of χ^2 and SHARP describes whether the image is more or less extended than the PSF. If the SHARP is close to 0, the object is likely to be a star; if it is significantly less than 0, the object is probably a corrupted pixel; and, if it is significantly larger than zero, the object is likely to be a galaxy or unresolved double star.

We matched the objects photometered in the R and V frames and determined the coordinate transformation between the frames. We derived the instrumental magnitudes with ALLFRAME (Stetson 1994), which simultaneously fits a PSF to objects in both colors using single positions and the coordinate transformation between frames. The input to ALLFRAME is a list of objects found in at least one frame. If ALLFRAME does not detect an object in both frames simultaneously, we eliminate it from further consideration.

The next step in the image reduction procedure is converting the instrumental magnitudes, R_{instr} and V_{instr} , to standard R and V magnitudes. We define aperture magnitudes, R_{ap} and V_{ap} , which are measured using the IRAF PHOT command with an aperture radius of 20 pixels and a sky annulus with inner and outer radii of 20 and 35 pixels. Curves of growth showed that this aperture is sufficiently large to include a constant fraction of the light independent of the known variability of the PSF. The instrumental, aperture, and standard magnitudes are related through the following equations:

$$V_{\text{ap}} = V_{\text{instr}} - a' = V + a + b(V - R) + cX \quad (1)$$

and

$$R_{\text{ap}} = R_{\text{instr}} - d' = R + d + e(V - R) + fX', \quad (2)$$

where X and X' are the average airmasses for the combined frames. The constants a' and d' are the zero-point offsets between the instrumental and aperture magnitudes for the V and R bands, respectively. Similarly, a and d are zero-point offsets between the aperture and standard magnitudes, b and e are the color correction coefficients, and c and f are the extinction coefficients.

To determine a' and d' for a given field, we measured aperture magnitudes with a radius of 20 pixels for the PSF stars on frames in which the neighbors of the PSF stars were subtracted (thus minimizing contamination). The average difference between the aperture magnitudes of the PSF stars and their corresponding instrumental magnitudes yields the values of the two offsets.

On each night of the photometric 1994 observing run, we imaged 33 standard stars (Landolt 1983, 1992) with $9.3 < V < 16.1$ and $0.1 < V - R < 1.5$. A least-squares fit of

equations 1 and 2 to the aperture magnitudes of the standards determined the coefficients of the transformation between aperture and standard magnitudes. Table 2 lists the values of the coefficients a through f which produce the best fit for a given night. We adopted the average color correction and extinction coefficients for the run, but use separate zero-points for each night. Adopting average zero-points resulted in unacceptably large scatter around the fitted relations. Substituting these coefficients and the average airmass values for a given field and band from Table 3 into equations 1 and 2 yields the standard magnitudes for the detected objects in all but the C0 and E1 fields, which were imaged during the non-photometric 1991 and 1993 observing runs, respectively.

On the second night of the 1994 observing run, we imaged in both V and R a tie field, E1(tie) (see Table 1), which overlaps the C0 and E1 fields. We identified the C0 and E1 PSF stars contained in the E1(tie) field, measured their aperture magnitudes in the E1(tie) frame, and derived their standard magnitudes with equations 1 and 2, setting the fitting coefficients a through f to the night 2 values (see Table 2). The instrumental magnitudes measured in the C0 and E1 fields for these selected PSF stars are also related to their derived standard magnitudes through equations 1 and 2 (combining a and a' and d and d' each into a single constant). The least-squares fit of equations 1 and 2 to these data yields sets of coefficients appropriate for the C0 and E1 fields. Substituting these coefficients in equations 1 and 2 yields standard magnitudes for the detected objects in the C0 and E1 fields.

Tables 4(a) through 4(i) present our final R - and V -band photometry for the C0, E1, SE1, W1, N2, E2, S2, SW2, and W2 fields, respectively. Only the beginning of Table 4(a) is shown in the printed version of this article to provide guidance on form and content. The entire tables appear in the electronic edition of the *Astronomical Journal*. The first five columns in the tables give the ID, x and y coordinates on the R frame, and α (J2000.0) and δ (J2000.0) for an object. The equatorial coordinates come from plate solutions based on positions for stars in the USNO-A2.0 catalog (Monet et al. 1998) using a recipe developed by Paul Harding (personal communication). Columns 6 and 7 give the R -band magnitude followed by its uncertainty, σ_R . Columns 8 and 9 list the same for the V band. The last two columns give the average CHI and SHARP values.

2.1. Comparison to Earlier Photometric Studies of Draco

There are two ground-based CCD photometric studies of Draco in the literature: Stetson et al. (1985; hereafter SVM) and Carney & Seitzer (1986; hereafter CS). Both groups imaged fields completely contained within our C0 field and both observed in the B and V bands. Therefore, we can only compare the V -band photometry from these studies to our

photometry.

SVM found 182 objects in their Draco fields; we matched 95 of these objects within a limit of 1 pixel. Figure 3 plots the magnitude difference $\Delta V \equiv V_{\text{us}} - V_{\text{SVM}}$ vs. V_{SVM} , where V_{us} is the magnitude determined in this study and V_{SVM} is the magnitude of the same object determined by SVM. CS imaged two fields in Draco: Field 1, where they found 1039 objects, and Field 2, where they found 875. We found 755 and 646 objects in common between our C0 field and Fields 1 and 2, respectively, within a limit of 1 pixel. We combined the two sets of objects into a single set from which we excluded those with $V < 18.0$ because CS note that their photometry of these objects is unreliable due to saturation. The final set consists of 1382 objects; however, since CS Fields 1 and 2 overlap by 26%, some objects appear twice in the final set. Figure 4 plots the magnitude difference, $\Delta V \equiv V_{\text{us}} - V_{\text{CS}}$ vs. V_{CS} , for 1382 objects. V_{CS} corresponds to the V -band magnitude determined by CS.

Figures 3 and 4 show small systematic offsets between the zero-points of the three studies for bright objects and a bias that causes ΔV to become progressively more negative with increasing magnitude starting at $V \simeq 21.0$. The unweighted mean offsets for objects brighter than $V = 21.0$ in Figures 3 and 4 are $\Delta V = 0.009 \pm 0.019$ and $\Delta V = -0.008 \pm 0.004$, respectively. The uncertainty in the mean offset is the rms scatter around the mean divided by the square root of the number of objects. For the data in Figure 4, the calculation of the mean offset and rms excluded the few points marked with a slanted cross. These correspond to some confirmed RR Lyrae stars from Baade & Swope (1961). However, we have made no attempt to identify all of the known RR Lyrae stars in our fields. The rms scatter around the mean offsets for the bright objects is 0.068 mag for the comparison with SVM and 0.061 mag for that with CS. The corresponding values of the χ^2 per degree of freedom are 4.472 and 2.375. These are larger than one at least in part because of unidentified variable stars, close pairs of stars resolved in one study and not the other, and galaxies photometered as stars.

The magnitude-dependent bias for fainter objects causes our magnitudes to be smaller on average than those determined by SVM and CS for corresponding objects. The direction of the bias is the same in both Figures 3 and 4, implying that its cause lies with our faint V -band C0 data. The SVM and CS data go much deeper than ours because they used 4 m telescopes. Near the faint limit of our photometry, we preferentially detect those objects made brighter by noise, but not those made fainter. This process produces a bias in the direction of that seen in Figures 3 and 4. While this process probably produces most or all of the bias for the faintest objects, it probably does not produce the bias for objects brighter than about magnitude 22. In this magnitude range, examining some cases suggests that close pairs of stars unresolved in our study cause the bias. We note that the C0 field has the shallowest photometry of any of our fields (see Sec. 2.3 below).

2.2. Comparison of Photometry from Overlapping Fields

Three pairs of our fields slightly overlap, E1 and C0, E1 and SE1, and S2 and SW2, allowing a comparison of photometry in both the R and V bands.

Figure 5(a) plots the magnitude difference $\Delta R \equiv R_{\text{E1}} - R_{\text{C0}}$ vs. R_{E1} for the 190 objects common to the E1 and C0 fields, matched to within 1 pixel. The figure shows a zero-point offset that extends over the entire range of magnitudes. Field E1 has the most variable focus among our images, as noted when discussing the stellar FWHMs in Table 1. Most of the objects showing the largest magnitude differences are located on the side of the overlap with the worst focus. At least one other large difference comes from a galaxy (the point near $R = 18.7$). Some of the scatter near $R \approx 20$ is probably due to RR Lyrae variables. The unweighted mean ΔR for objects brighter than $R_{\text{E1}} = 21$ is -0.026 ± 0.010 , excluding the discrepant points discussed above. We attribute this large mean difference to the variable focus in field E1.

Figure 5(b) plots the magnitude difference $\Delta V \equiv V_{\text{E1}} - V_{\text{C0}}$ vs. V_{E1} for the same 190 objects. This figure also shows a zero-point offset, though in the opposite direction to that in Figure 5(a). The discrepant points have the same cause as those in the R -band comparison. The unweighted mean ΔV for objects brighter than $V_{\text{E1}} = 21.5$ is $+0.010 \pm 0.010$, excluding the most discrepant points. Again, the magnitude difference depends on position along the overlap and is most discrepant in the region where the focus in E1 is the worst.

Figure 6(a) plots the magnitude difference $\Delta R \equiv R_{\text{E1}} - R_{\text{SE1}}$ vs. R_{E1} for the 54 objects common to the E1 and SE1 fields, matched to within 1 pixel. A bad column in the E1 image affects the comparison. The unweighted mean ΔR for objects brighter than $R_{\text{E1}} = 22.0$ is -0.005 ± 0.015 , excluding the two most deviant points (produced by objects on the bad column). As with the comparison of E1 and C0, the magnitude difference depends on position within the overlap region – an effect due to focus variations in E1.

Figure 6(b) plots the magnitude difference for the same 54 objects in the V band. The unweighted mean ΔV for objects brighter than $V_{\text{E1}} = 22.0$ is -0.013 ± 0.020 , excluding one discrepant point corresponding to an object on the bad column.

Both sets of comparisons with the photometry of the E1 field show that the focus variations cause offsets in the zero-points at the level of a few hundredths of a magnitude. These offsets do not significantly affect our conclusions, partly because we remove color offsets between the data from different fields. This is discussed in Sec. 3. However, the focus variations in E1 do affect our ability to differentiate between stars and galaxies and, for this reason, we exclude this field from some of our analyses.

Figure 7(a) plots the magnitude difference $\Delta R = R_{S2} - R_{SW2}$ vs. R_{S2} for the 83 objects common to the S2 and SW2 fields, matched to within 1 pixel. The discrepant point near $R_{S2} = 18$ corresponds to a galaxy. Excluding this point, the unweighted mean ΔR for objects brighter than $R_{S2} = 22.0$ is $+0.007 \pm 0.014$.

Figure 7(b) plots the magnitude difference for the same 83 objects in the V band. The unweighted mean ΔV for objects brighter than $V_{S2} = 22.0$ is $+0.015 \pm 0.012$, excluding the same galaxy and the next most discrepant point. The latter is due to an object only partly within the field. The good agreement between the photometry from the S2 and SW2 fields suggests that most of our data has a consistent zero-point.

The comparison of the photometry from overlapping fields shows that the zero points of our different fields could differ by approximately 0.01 mag. The comparison with SVM and CS suggests that the zero points of their and our studies are also uncertain at the 0.01 mag level.

2.3. Completeness

To ascertain the completeness of our photometry as a function of magnitude, we performed artificial star tests for all of the Draco fields.

In each test, we added 600 artificial stars to both the R and V frames at random positions. This number of artificial stars is 10% or less of the total number of objects in a field. The added stars have the profile of the PSF for the given frame. We reduced the frames following the same procedure as for the original frames. The artificial stars are recovered by matching their known input positions with those of the recovered objects both artificial and real.

For a given field, we performed six simulations. In each of the first three simulations, we added a total of 600 artificial stars to a frame, 200 for each of the following pairs of R and $V - R$: 22.1 and 0.368; 22.6 and 0.288; and 23.1 and 0.257. The second three simulations are identical except that they used R and $V - R$ pairs of: 23.35 and 0.258; 23.6 and 0.265; and 23.85 and 0.276. We chose the R and $V - R$ pairs from an isochrone with $[\text{Fe}/\text{H}] = -2.0$ and an age of 14 Gyrs taken from McClure et al. (1987), shifted to the distance and reddening of Draco given in Webbink (1985) using the relation between $E(B - V)$ and $E(V - R)$ from Cardelli et al. (1989) (i.e., apparent $(m - M)_R = 19.46$ and $E(V - R) = 0.02$).

Table 5 lists the average recovery percentages of the artificial stars for each Draco field as a function of R . The uncertainties are the rms scatter of the three simulations. With the

exception of the C0 field, the recovery is almost complete up to $R=22.6$, with field-to-field variations of about 2.5% or less. The small loss of artificial stars is caused by mergers with saturated objects, which ALLFRAME eventually rejects. Of course, an artificial star could also merge with an object which is not saturated, though most likely faint. We checked the likelihood of this by matching the input positions of the artificial stars with the original positions of the objects from Table 4. We found that only a few artificial stars are sufficiently close to the objects for mergers to occur. Since the artificial star is recovered and the object it has merged with is probably faint, we decided to include such recoveries in our recovery percentages.

For $R = 23.1$ and fainter, the completeness percentages are well below 100% and their field-to-field variations become substantial.

3. Color-Magnitude Diagrams

The objects listed in Tables 4(a) through 4(i) are a combination of Draco stars, foreground Galactic disk and halo stars, background galaxies, and a few spurious objects due to bad pixels or charge overflow columns. The expected surface density of Draco stars beyond the tidal boundary is smaller than the total foreground and background surface density. Thus, our search for such Draco stars is more sensitive if we can use additional information to eliminate other objects from the sample. This section discusses the two pieces of information that we use: the morphology of the images and the location of objects on the color-magnitude diagram.

Two quality-of-fit parameters of DAOPHOT, CHI and SHARP (described in Sec. 2), permit some discrimination between the objects. Figure 8 is a plot of the R -band magnitude vs. SHARP for the C0 field. Figure 8 shows three distinct groups of points. First, a bright, horizontal group with $R \lesssim 16$ whose SHARP values are widely scattered. These are saturated stars or spurious objects on charge overflow columns with CHI values larger than 5.0. We eliminate these from all samples discussed subsequently. Second, a vertical group whose SHARP values are near zero for objects brighter than $R \simeq 22$. For fainter objects, the scatter in the values increases because of the decreasing signal-to-noise and becomes very wide fainter than $R \simeq 23$. Most of the brighter objects in this group are stars; at fainter levels they become mixed with the third group – galaxies. The extended images of galaxies have larger SHARP values than those of stars, allowing the two groups to be distinguished until a decreasing signal-to-noise causes the two groups to overlap, as depicted in Figure 8. For objects fainter than $R = 21$, exact differentiation between the two groups based on SHARP values becomes impossible.

The lines in Figure 8 show the SHARP limits that we have adopted to separate stars from galaxies. We set these limits symmetrically about zero to include nearly all of the objects with negative SHARP values, which are not contaminated by galaxies. Thus, “stars” must have SHARP values within 0.25 of zero for $R < 21.0$; within limits increasing linearly to ± 0.50 at $R = 22.0$; and within limits increasing linearly to ± 1.00 at $R = 23.0$. For objects fainter than $R = 23.0$, we allow any value of SHARP. In our analysis, we will apply these limits to the data for all of our fields.

Figure 9 shows color-magnitude diagrams (CMDs, hereafter) plotting R vs. $V - R$ for our nine fields. The R - and V -band magnitudes are from Tables 4(a) through 4(i). We only plot objects with CHI values less than 5.0 and SHARP values within the limits shown in Figure 8.

The CMD for the C0 field clearly shows the principal sequences of Draco: in particular, the horizontal branch (HB, hereafter) and red giant branch (RGB, hereafter). The distribution of stars on the HB is somewhat distorted by RR Lyrae stars in Draco with incorrectly measured colors due to the lack of phase coverage in our data. The effect is particularly noticeable for C0 because the R - and V -band images are from different nights.

The CMDs for the E1 and W1 fields also show the HB and RGB, as expected, since more than 50% of both fields are within the measured tidal boundary of Draco (see Figure 1).

No easily discernible Draco principal sequences appear on any of the remaining CMDs. However, this should not be construed as categorical proof for the absence of Draco stars in these fields. Instead, it is only certain that these fields have fewer Draco stars than the C0, E1, and W1 fields.

Excluding the features due to Draco stars in the CMDs for the C0, E1, and W1 fields, all of the CMDs display a very similar and complex morphology produced by Galactic field stars. A sharp blue edge to the distribution of points is one of the most conspicuous features seen on the CMDs. It is due to the main-sequence turnoff of Galactic field stars smeared in apparent magnitude by the range of distances along the line of sight (e.g., Reid & Majewski 1993). Disk stars populate mostly the upper part of the blue edge due to the finite thickness of the disk, whereas the more distant halo stars occupy the lower part. Intrinsically fainter main sequence disk stars produce the band of points extending to the red from the disk turnoff region to the concentration of points between $V - R = 1.0$ and 1.5, which is due to the numerous disk stars on the lower main sequence. The large number of points at the bottom of each CMD represent both stars and galaxies not rejected by the increasingly loose SHARP limits required by the larger photometric uncertainties.

The color of the blue edge should be the same in all of our CMDs. It is not. One

possible reason for this is differential reddening due to interstellar dust. Figure 10 shows the location of our fields superimposed on a map of the reddening, $E(B - V)$, derived from dust infrared emission by Schlegel et al. (1998). From this map, we calculated the average reddening for each field; these are listed in column two of Table 6. We adopt an average reddening for each field instead of correcting each object individually because the reddening does not vary strongly across our fields and the resolution of the map is comparable to the size of our fields. Multiplying the $E(B - V)$ values for each field by 2.673 and 3.315 (Schlegel et al. 1998; the Landolt values from their Table 6) gives the extinction in the R band, A_R , and V band, A_V , respectively. Table 6 lists these values in columns 3 and 4, respectively.

The fifth column of Table 6 lists the measured color of the blue edge for all of the fields after correcting for interstellar reddening and extinction. We estimated these colors by counting the number of points in a sliding rectangular box in the dereddened CMD. The box is 0.1 mag wide in color and extends from $R = 19$ to $R = 14$. As the box slides from $(V - R)_0 = 0$ to $(V - R)_0 = 0.4$ in 0.025 mag steps, the number of points in the box rapidly increases as it crosses the blue edge. We normalize the numbers with respect to the highest value and adopt as the location of the edge that color where the normalized number is 0.5.

The C0 field has the bluest edge ($(V - R)_0 = 0.240$), the W2 field has the reddest ($(V - R)_0 = 0.340$), and the rest of the fields have values roughly clustered around a mean of $(V - R)_0 = 0.304$. The difference in the extreme values is visible by eye on the CMDs and is significantly larger than the 0.007 mag average measurement uncertainty estimated from a Monte Carlo simulation. The variation in the edge colors is likely due to errors in the photometric zero points and is consistent with the zero-point differences shown in Figures 5 – 7 for objects located where fields overlap; see the discussion in Sec. 2 for details.

Figure 11 shows a CMD for the C0 field with no corrections made for extinction. The solid lines outline the region where the principal sequences of Draco are located. Magnitude $R = 16.4$ bounds this region at the top and $R = 23.4$ (the approximate limit to which the photometry has completenesses greater than 50%, see Table 5) at the bottom. The photometric uncertainty in $V - R$ determines its horizontal width for objects brighter than $R = 22.6$ — we adopted $\pm 3\sigma_{V-R}$. Fainter than this limit, the width increases only slightly to keep the region from including nearly all objects. The crosses near the $R = 20$ mag level correspond to some confirmed RR Lyrae stars from Baade & Swope (1961), validating the assertion that the distribution of stars on the HB is somewhat distorted by the variability of RR Lyrae stars. We did not attempt to identify, or to confirm, all of the possible RR Lyrae stars in our fields because our data is too sparsely sampled in time to do so effectively.

We evaluate and classify every object in every field based on its CHI and SHARP values and where it is positioned on a CMD. The latter evaluation must be done in a consistent

photometric system. We adopt the photometry of the C0 field, not corrected for extinction, as this system in this article. Thus, the R -band magnitude of every object is adjusted by the difference between the A_R for its field and that for C0. The $V - R$ of every object is adjusted by the difference in the reddenings and by the difference in the reddening-corrected colors of the blue edge.

Objects divide themselves into two categories depending on their positions in the CMD with respect to the region outlined in Figure 11. An object is “in” if it lies within the region and it is “out” if it lies outside of the region.

4. Searching for Draco Stars — Methods and Results

In this article we use three methods to search for Draco stars beyond the measured tidal boundary of the dSph. 1) Plotting color-magnitude diagrams for combinations of fields and sections of fields and looking for the principal sequences. 2) Measuring the field-to-field and 3) intra-field fluctuations in the surface density of objects selected from the “in” and “out” regions of the CMD defined in the previous section.

Each of the above methods makes different assumptions and has its own strengths and weaknesses. The first method makes no assumptions about the distribution of Draco stars on the sky. However, there must be enough of these stars in the regions examined to make the principal sequences visible in the CMD. The necessity of recognizing the principal sequences makes this method somewhat subjective. The other two methods assume that the Draco stars beyond the tidal boundary have an irregular distribution on the sky. The second method searches for irregularities in the distribution on an angular scale comparable to the separation between fields, while the third looks for irregularities on a scale comparable to the angular size of an individual field. Unlike the first method, these two methods are objective and can produce quantitative estimates of the number of Draco stars present. However, they cannot find Draco stars uniformly distributed among all of the fields — such as a symmetric halo of uniform density. We search for irregularities using the surface density of objects from the “in” region of the CMD, Σ_{in} . Another weakness of the second and third methods is that fluctuations in the number of foreground and background objects can mask those in the Draco stars. To judge the size of the fluctuations of foreground and background objects, we examine the surface density of “out” objects, Σ_{out} . We will calculate Σ_{in} and Σ_{out} to many limiting magnitudes. If no limit is stated, it is $R = 22.6$, the limit to which our photometry is nearly complete. We also examine the ratio $\Sigma_{\text{in}}/\Sigma_{\text{out}}$, a quantity less sensitive to the correlation between Σ_{in} and Σ_{out} caused by the large contribution of field objects to Σ_{in} . We discuss this complex issue further below.

The following three subsections present our implementation of the three methods in more detail and describe the results of the search for Draco stars. The reader may wish to read the summary of the results in Section 5 before reading the following subsections.

4.1. Principal Sequences in the CMD

If Draco stars are present in a given field, they will lie close to the principal sequences of Draco in the CMD. The CMDs for the fields outside of the tidal boundary of Draco, depicted in Figure 9, do not show such sequences. It is especially surprising not to see them in the CMD for the SE1 field, whose northwest corner is inside of the measured tidal boundary of Draco (see Figure 1). As we remarked above, the apparent absence of the sequences in a CMD does not mean that there are zero Draco stars in this field; instead, it poses the question: How close is the number to zero?

If there are small numbers of Draco stars present in individual fields, combining the data into a single CMD may increase the visibility of the principal sequences. If Draco stars are not uniformly distributed either within or between fields, it will be more advantageous to combine just the data from the regions where the Draco stars are most numerous. One approach is to select the fields and sections of fields by trial and error to maximize the visual appearance of the principal sequences. Another is to select quadrants of fields having larger-than-average values of Σ_{in} or $\Sigma_{\text{in}}/\Sigma_{\text{out}}$. These are the two approaches that we take in this article.

Sections of the E1, SE1, and W1 fields are outside of the tidal boundary of Draco (see Figure 1). Figure 12(a) is a CMD for the combined set of objects within these sections. For comparison, Figure 12(b) shows the CMD for the C0 field plotted with the same scale. These CMDs, and the others that follow, show only those objects satisfying the CHI and SHARP criteria described in Sec. 3. In addition, all data have been shifted to the photometric system of the C0 field. The CMD in Figure 12(a) shows only very weak evidence for the presence of Draco stars: a small clump of points in the HB region ($R \approx 20$, $V - R \approx 0.25$) and a faint lower RGB. Both features could occur by chance due to a small number of points in those regions of the CMD. However, Figure 12(c) shows that adding the objects from the E2 and W2 fields to the data in Figure 12(a) makes the principal sequences visually more prominent. In contrast, Figure 12(d) shows that adding the objects from the N2, S2, and SW2 fields to the data in Figure 12(a) does not have the same effect.

Admittedly, the presence or absence of the principal sequences of Draco in Figures 12(a), (c), and (d) is subjective. The human eye is better suited to discerning very weak structural

features in gray-scale images than on a scatter plot, especially if the number of points is small. Thus, to make the decision more objective, we replot Figure 12 as gray-scale Hess diagrams in Figure 13. We calculated the density of points in these diagrams on a 150×150 pixel grid using a fixed-width kernel of the form $(1 - (\Delta R/w_R)^2 - (\Delta(V - R)/w_{V-R})^2)^2$. Here ΔR and $\Delta(V - R)$ are the distances of the point from the center of a pixel in R and $V - R$, respectively, and w_R and w_{V-R} are two constants that determine the width of the kernel. For Figure 13(a), $w_R = 0.075$ and $w_{V-R} = 0.30$, while for Figures 13(b), (c), and (d) $w_R = 0.062$ and $w_{V-R} = 0.25$. In Figure 13, white corresponds to zero density and black to 35% of the peak density. The contour in Figures 13(a), (c), and (d) is an isopleth from Figure 13(b) and outlines the principal sequences of Draco. Figures 13(a) and (c) show density enhancements at the expected locations of the HB and, less prominently, the lower RGB. In contrast, Figure 13(d) does not.

Panels (a) and (c) of Figures 12 and 13 imply that there are Draco stars beyond the tidal boundary measured by IH. Panels (c) and (d) of Figures 12 and 13 show that fewer, possibly no, Draco stars are present in the N2, S2, and SW2 fields, implying an irregular azimuthal distribution for the Draco stars beyond its measured tidal boundary. If there are Draco stars in the E2 and W2 fields, as Figures 12(c) and 13(c) suggest, then these stars are at least 60 arcmin away from the center of Draco approximately along the extension of its major axis.

Taking our alternative approach, we select quadrants from our fields that are entirely beyond the measured tidal boundary and have values of Σ_{in} and $\Sigma_{\text{in}}/\Sigma_{\text{out}}$ larger than the average. This procedure excludes all quadrants in the C0, E1, and W1 fields and the northwest quadrant of the SE1 field. If high values of Σ_{in} and $\Sigma_{\text{in}}/\Sigma_{\text{out}}$ are indicative of the presence of Draco stars, the CMD for the data from these regions should show the principal sequences. Figure 14(a) is the CMD for the quadrants with higher than average Σ_{in} : SE1 - northeast; N2 - northwest; E2 - northeast, southwest, and southeast; SW2 - northeast, southwest, and southeast; W2 - northeast and southwest. Figure 14(c) is its corresponding gray-scale Hess diagram, calculated as for Figure 13 with kernel widths of $w_R = 0.062$ and $w_{V-R} = 0.25$. Figure 14(b) is the CMD for the quadrants with higher than average $\Sigma_{\text{in}}/\Sigma_{\text{out}}$: SE1 - northeast; N2 - northeast and northwest; E2 - northeast and southwest; SW2 - northeast; W2 - northeast, northwest, and southwest. Figure 14(d) is its gray-scale Hess diagram. The contour in both Figures 14(c) and (d) is the same as that in Figure 13(a). None of these figures shows the principal sequences as clearly as Figures 12(c) and 13(c). There are clumps of points in the general vicinity expected for the HB, but Figures 14(c) and (d) show that these are brighter than expected for Draco HB stars. Thus, either the number of Draco stars in the quadrants entirely beyond the tidal boundary is too small, or the fluctuations in the number of field objects in those quadrants is too large, for Σ_{in} or $\Sigma_{\text{in}}/\Sigma_{\text{out}}$ to be a good

indicator of the presence of Draco stars.

We have tried many other combinations of quadrants and entire fields, both with and without the regions of E1 and W1 outside of the measured tidal boundary, and none show the principal sequences more clearly than Figures 12(c) and 13(c).

In conclusion, we have found evidence for Draco stars beyond the tidal boundary measured by IH. The distribution of these stars is uncertain, but they may extend as far as 1.3 degrees from the center of Draco.

4.2. Surface Density Fluctuations

If the surface density of Draco stars beyond the measured tidal boundary is non-uniform on a scale comparable to the angular separation between the fields, then the value of Σ_{in} should fluctuate from field to field. If these fluctuations are due to Draco stars, then the field-to-field fractional rms scatter around the mean Σ_{in} should increase with the limiting magnitude of the sample because of the rapid increase in the number of stars along the RGB. However, field objects, whose projected distribution can be non-uniform too, make the largest contribution to Σ_{in} . Therefore, it is imperative to check for other causes for the fluctuations in Σ_{in} . To help with this, we measure the fractional rms scatter around the mean Σ_{out} and, additionally, around the mean $\Sigma_{\text{in}}/\Sigma_{\text{out}}$, both as a function of limiting magnitude. However, we caution that it is possible that the mixture of disk stars, halo stars, and background galaxies that contribute to Σ_{in} could fluctuate differently from those that contribute to Σ_{out} . Despite this, significant fluctuations in Σ_{out} would suggest the potential for fluctuations in Σ_{in} due to field objects.

Galaxies are clustered on the sky and thus contribute to the fluctuations in both Σ_{in} and Σ_{out} . We can partially exclude galaxies from our data sets based on how well an object matches the stellar PSF, as discussed in Sec. 3. If this exclusion significantly reduces the size of the fluctuations, it would suggest that there is a potential for galaxies to still cause fluctuations in Σ_{in} , since we know that not all galaxies can be eliminated. This problem is greatest for the faintest objects, whose low signal-to-noise ratio makes galaxy-star separation impossible.

The panels in Figure 15 plot the fractional rms scatter around the mean of Σ_{in} , Σ_{out} , and $\Sigma_{\text{in}}/\Sigma_{\text{out}}$ measured in seven regions as a function of limiting magnitude. These are shown as solid points and should be compared with the scatter expected from Poisson noise, shown as open squares. The seven regions are: SE1 (excluding the small section within the measured tidal boundary), W1 (also excluding the section within the tidal boundary),

N2, E2, S2, SW2, and W2. We exclude the entire E1 field from this figure because the large focus variations seriously degrade the galaxy-star separation. However, we did not exclude E1 in the discussion of CMDs because the increase in the contamination by galaxies does not significantly affect the detection of the principal sequences. The error bar shown for the measured fractional rms scatter is the sampling uncertainty for a sample of seven measurements. To indicate the contribution of galaxies to the rms scatter, the left-hand panels use all objects, regardless of their SHARP and CHI values, while the right-hand panels exclude objects which either have CHI values larger than 5.0 or SHARP values outside of the limits shown in Figure 8.

Figure 15(a) plots the fractional rms scatter in Σ_{in} as a function of limiting magnitude for all objects, regardless of their SHARP and CHI values. The figure shows that the field-to-field fluctuations in Σ_{in} are larger than those expected from Poisson noise for all limiting magnitudes. Figure 15(b) is the corresponding plot for Σ_{out} , though note the different vertical scale. The field-to-field fluctuations in Σ_{out} are also larger than those expected from Poisson noise, though generally smaller than those for Σ_{in} . Around $R = 22.2$, the fluctuations in Σ_{out} begin to increase with limiting magnitude and exceed those in Σ_{in} . This increase is due to the progressively larger contribution from galaxies with increasing magnitude; a particularly large contribution comes from the SW2 field, which contains an x-ray galaxy cluster (Zwicky 8197; Ebeling et al. 1998). Replotting the figure excluding the SW2 field reduces the fluctuations significantly, though they still generally remain larger than Poisson noise. Unequal completeness for the different fields could also contribute to the increase in the fluctuations for the faintest limiting magnitudes, though its contribution is probably small since Figure 15(a) does not show a comparable increase.

Figure 15(c) plots the fractional rms scatter in $\Sigma_{\text{in}}/\Sigma_{\text{out}}$ as a function of limiting magnitude. The pluses are the values expected for the observed fractional rms scatter if the scatters in Σ_{in} and Σ_{out} are uncorrelated, i.e., they add in quadrature. All of the observed points, the solid squares, are below the pluses. This result shows that fluctuations in Σ_{in} and Σ_{out} are correlated. We conclude that the fluctuations in Σ_{in} seen in Figure 15(a) are not solely attributable to Draco stars beyond the measured tidal boundary. Instead, field stars and galaxies must contribute to these fluctuations. We can partially remove the contribution from galaxies by excluding objects based on their values of CHI and SHARP; however, there is no similar way to remove the contribution from field stars. The right-hand panels of Figure 15 show the corresponding plots with the galaxies partially removed.

Figure 15(e) shows that fluctuations in Σ_{out} are comparable with Poisson noise up to about $R = 22.4$. At fainter limiting magnitudes, the fluctuations begin to increase as in Figure 15(b) — a reflection of looser SHARP limits (see Figure 8) and the galaxy cluster

in the SW2 field. Again, excluding the data from the SW2 field reduces this increase. Comparing Figures 15(b) and (e) shows that removing galaxies from the data has reduced the field-to-field fluctuations in Σ_{out} for all limiting magnitudes and, for $R < 22.4$, reduces it to the level of Poisson noise. Based on this comparison, field stars do not cause significant fluctuations in Σ_{out} , suggesting that they are not likely to cause them in Σ_{in} either.

Comparing Figures 15(a) and (d) shows that removing galaxies from the data has reduced the field-to-field fluctuations in Σ_{in} for all limiting magnitudes, but not to the level of Poisson noise. This contrast with Figures 15(b) and (e) argues that significant fluctuations remain, most likely due to the presence of Draco stars beyond the measured tidal boundary. Note that the points in Figure 15 are not independent; hence, the statistical significance of the deviation from Poisson noise must be evaluated at only a few points. Replotting Figure 15(d) excluding the objects from the W1 field shows fluctuations that are comparable to the expected Poisson noise, arguing that the objects from the section of the W1 field beyond the measured tidal boundary have the greatest contribution to the fluctuations seen in Figure 15(d). The fluctuations in the number of Draco stars in the more distant fields cannot be larger than those expected from Poisson noise, though they might still be present. We conclude that there are Draco stars in the region of the W1 field beyond the tidal boundary measured by IH. However, we do not find clear evidence from the fluctuations of Σ_{in} to support the suggestion from the CMDs in Sec 4.1 for Draco stars at larger radii.

Figures 15(d) and (f) show that the fluctuations in $\Sigma_{\text{in}}/\Sigma_{\text{out}}$ are closer to those expected from Poisson noise than the fluctuations in Σ_{in} . This is probably due to the increased Poisson noise contributed by Σ_{out} , which dilutes the signal of Draco stars beyond the tidal boundary from Σ_{in} . Figure 15(f) shows that removing galaxies from the data has reduced the correlation between fluctuations in Σ_{in} and Σ_{out} for all limiting magnitudes. Only fainter than a limiting magnitude of $R = 22.6$ does the correlation become significant. The likely causes of this are unequal completeness between fields and faint galaxies whose SHARP values are within the loosening limits shown in Figure 8.

Figure 15 shows that galaxies produce significant and correlated fluctuations in Σ_{in} and Σ_{out} . Eliminating objects based on their SHARP and CHI values reduces these correlations to statistically insignificant levels for all limiting magnitudes for which our data are complete. Significant fluctuations remain only in Σ_{in} for limiting magnitudes brighter than $R = 22.6$. We attribute these to the presence of Draco stars beyond the measured tidal boundary, particularly in the W1 field.

Table 7 and Figure 16 provide information on Σ_{in} , Σ_{out} , and $\Sigma_{\text{in}}/\Sigma_{\text{out}}$ for each field at the limiting magnitude for which our photometry is complete, $R = 22.6$. Table 7 has three blocks: the first lists the surface area of the field in square arcmin; the second lists

the values of the two surface densities in objects per square arcmin and their ratio for all objects, regardless of their SHARP and CHI values; the third block is the same as the second for objects with CHI values less than 5.0 and SHARP values within the limits depicted in Figure 8. We list two uncertainties below each surface density or ratio entry: the internal uncertainty, σ_{int} , and the external uncertainty, σ_{ext} . The first is the Poisson noise and the second is the estimate based on the rms scatter around the mean value for the four quadrants of the field. The last three columns of the table give 1) the mean value of the two surface densities or their ratio and the rms scatter around this mean calculated for the sets of fields described in the notes to the table; 2) the two χ^2 values for the scatter around each mean calculated with σ_{int} and σ_{ext} ; and 3) the probability of exceeding each χ^2 value by chance.

The top three panels of Figure 16 plot, from left to right, Σ_{in} , Σ_{out} , and $\Sigma_{\text{in}}/\Sigma_{\text{out}}$ for a selection of fields from the second block of Table 7. The middle three panels are the same plots for data from the third block of Table 7. In these six panels, the error bars on all of the points are σ_{int} . The bottom three panels are the same as the middle panels, except that the error bars are σ_{ext} . For each column of panels, the ordinates have the same fractional range of values to simplify the visual comparison of fractional scatters. We exclude from the figure fields C0 and E1. C0 falls entirely within the tidal boundary and also contains an unusually large number of spurious objects which compromise Σ_{out} . E1 has a variable focus which compromises Σ_{in} and Σ_{out} . The figure includes the section of field W1 beyond the tidal boundary, denoted as W1* on the abscissa. The values for this section are not in Table 7; they are for the top panels: $\Sigma_{\text{in}} = 2.79 \pm 0.12$, $\Sigma_{\text{out}} = 4.53 \pm 0.15$, and $\Sigma_{\text{in}}/\Sigma_{\text{out}} = 0.615 \pm 0.032$ and for the middle panels $\Sigma_{\text{in}} = 1.902 \pm 0.095$, $\Sigma_{\text{out}} = 3.19 \pm 0.12$, and $\Sigma_{\text{in}}/\Sigma_{\text{out}} = 0.596 \pm 0.038$. Figure 16 plots values for the entire SE1 field because the portion within the tidal boundary is small — excluding this portion has a negligible effect on the values.

The top three panels in Figure 16 show the large scatter among fields that causes the values of the fractional rms to be larger than that expected from Poisson noise at $R = 22.6$ in the left-hand panels of Figure 15. The high value of Σ_{out} for the SW2 field is due to galaxies from the cluster Zwicky 8197. This cluster extends into the S2 field, also raising its Σ_{out} . Eliminating objects based on their SHARP and CHI values reduces the scatter among fields as shown in the middle row of panels. This is reflected in the reduction of the χ^2 values calculated with σ_{int} between blocks two and three of Table 7. In the middle row of panels, the W1* field has the highest value of Σ_{in} and of $\Sigma_{\text{in}}/\Sigma_{\text{out}}$ and a value of Σ_{out} comparable to those for the other fields. This demonstrates that this region contains Draco stars.

Excluding W1*, the middle row of panels still shows more scatter than expected from Poisson noise and this is confirmed by the χ^2 values and their probabilities in the third block

of Table 7. Is this evidence for Draco stars in these fields? It is at best weak evidence, since this scatter is larger for Σ_{out} than for Σ_{in} and the scatter in Σ_{in} has a 9% probability of being caused by Poisson noise. Though the scatter in Σ_{in} could be caused by Draco stars, we judge that this is unlikely because of the significant fluctuations in Σ_{out} , which cannot be caused by Draco stars. Other possible sources for fluctuations in either surface density are differences in image quality that affect the rejection of objects based on their CHI and SHARP values and the clustering of faint galaxies that cannot be rejected because of their low signal-to-noise ratio.

The bottom row of panels in Figure 16 and the χ^2 values calculated with σ_{ext} in Table 7 test if the fluctuations among fields are caused by the clustering of galaxies or field stars on scales comparable to the size of a single field. These χ^2 values in the second block of Table 7 show that there are significant fluctuations within fields for all objects without regard to their CHI and SHARP values. In contrast, these χ^2 values in the third block are not significantly different from those calculated with σ_{int} — the scatter of the surface densities and their ratio shown in the bottom panels of Figure 16 are still larger than the error bars. We conclude that this scatter is due to differences among fields, either in the surface densities of galaxies or stars or in the ability to reject objects on the basis of their CHI and SHARP values. Unfortunately, we cannot quantify these different contributions and so we can only place an upper limit on the fluctuations due to Draco stars — the rms scatter around the mean Σ_{in} given in the third block of Table 7.

4.3. Intra-field Fluctuations

If the Draco stars beyond the measured tidal boundary have a non-uniform distribution on an angular scale comparable to that of a single field, then σ_{ext} should be larger than σ_{int} for Σ_{in} and $\Sigma_{\text{in}}/\Sigma_{\text{out}}$ while comparable for Σ_{out} . Blocks 2 and 3 in Table 7 list these uncertainties. The presence of Draco stars in the C0, E1, and W1 fields is evident in Table 7, which shows that σ_{ext} is larger than σ_{int} in the second and third blocks. The difference in size is largest for Σ_{in} and $\Sigma_{\text{in}}/\Sigma_{\text{out}}$. While σ_{ext} is larger than σ_{int} for Σ_{out} , the difference is only statistically significant for E1, which has a PSF that varies strongly across the field (see Sec. 2).

The relative sizes of the values for σ_{int} and σ_{ext} listed in the second block of Table 7 show that there are significant fluctuations in both surface densities and in their ratio on the scale of a single field. However, except for the fields C0, E1, and W1, the values in the third block of Table 7 show no statistically significant differences. Thus, we attribute the larger σ_{ext} in the second block to the presence of galaxies (note the large values of σ_{ext} for

the SW2 field) and conclude that comparing σ_{int} and σ_{ext} provides no evidence for Draco stars beyond the measured tidal boundary.

5. Summary and Discussion

The presence of principal sequences in the CMD (Figures 12 (a) and 13(a)) for the regions of the E1, W1, and SE1 fields beyond the tidal boundary measured by IH demonstrate the presence of Draco stars in at least some of these regions. The value of Σ_{in} for the region of W1 beyond the measured tidal boundary confirms that Draco stars are in this region. We think that the CMDs shown in Figures 12(c) and 13(c) provide evidence (primarily in the visibility of the HB) that the Draco stars extend into the more distant fields E2 and W2. However, we acknowledge that others may disagree because the principal sequences are present only at the level of the noise. The field-to-field scatter in the values of Σ_{in} for the more distant fields is comparable to that of Σ_{out} and so the values of Σ_{in} can neither prove nor disprove the presence of Draco stars at these larger radii. A confirmation of the membership of these stars must come from other techniques, such as measurements of radial velocity, proper motion, metallicity, or luminosity.

If there are Draco stars in our E2 and W2 fields, this implies that the surface density of Draco decreases with increasing radius much more slowly beyond a radius of about 30 arcmin than between 10 and 20 arcmin. Models of the tidal stripping of stars from a dSph produce such a break in the profile at the approximate radius where the stars change from being mostly bound to mostly unbound (e.g., Johnston et al. 1999). If this interpretation is correct, the stars at large radii should have a mean velocity above that of Draco on one side and below on the other (Oh et al. 1995; Piatek & Pryor 1995; Klessen & Kroupa 1998; Johnston et al. 1999). Until such measurements exist, alternative explanations are also viable. For example, the creation of a spatially extended population of bound stars either during the formation of the dSph or later when gas was driven to large radii by stellar winds or supernovae. Gas is seen in large shells around some dwarf irregular galaxies (Puche & Westpfahl 1994).

The greater visibility of the principal sequences in the CMDs of Figures 12(c) and 13(c) compared to those of Figures 12(d) and 13(d) indicates that any Draco stars present at large radii concentrate mainly to the east and west of the galaxy. This suggests that the stars beyond the measured tidal boundary are along extensions of the major axis, but demonstrating this requires data with more complete azimuthal coverage.

We find that searching for Draco stars through fluctuations in the surface densities of

objects in fields where the expected number of these stars is small compared to the numbers of foreground field stars and background galaxies is subject to significant uncertainties. The left-hand panels of Figure 15 show that galaxies produce fluctuations larger than expected from Poisson noise over a broad range of limiting magnitudes, thus potentially masking fluctuations due to Draco stars. Removing objects based on the morphology of their images can greatly reduce these fluctuations (see the right-hand panels of Figure 15). However, this procedure cannot be completely effective, particularly when applied to objects with low signal-to-noise ratios, and can introduce spurious fluctuations if the focus or seeing varies among fields.

We estimate the surface density of Draco stars beyond the measured tidal boundary using the Σ_{in} values from the third block of Table 7 and the equivalent value for the W1 field given in the text. The most reliable estimate is for this region of the W1 field. The difference between the Σ_{in} for this region and the mean value for the SE1, N2, E2, S2, SW2, and S2 fields, given in Table 7, yields 0.30 ± 0.10 stars arcmin⁻², while using the lowest Σ_{in} , that for the SE1 field, instead of the mean yields 0.39 ± 0.11 stars arcmin⁻². The comparison of these values with those of IH and with theoretical models requires that they be expressed as a fraction of the central surface density of Draco.

To calculate a central surface density of Draco, we derived its density profile along the major axis in the C0 field by counting in elliptical annuli those objects that contribute to the Σ_{in} listed in the third block of Table 7. The ellipticity and position angle of these annuli are from IH. The greater incompleteness of the C0 field (see Table 5) was approximately corrected by multiplying the number of objects between $R = 22.1$ and 22.6 (38% of the total number) by $0.95/0.80 = 1.19$. The resulting profile agrees well with that of IH and yields a central surface density of 20.0 ± 1.4 stars arcmin⁻². The Poisson uncertainties in the binned densities account for most of the uncertainty in this value. We will present the radial density profile for Draco based on the data from all of our fields elsewhere (Piatek et al. 2000).

Our estimate of the surface density of Draco stars in the W1 field beyond the measured tidal boundary is thus 0.015 ± 0.005 to 0.020 ± 0.006 of the central density. This estimate is within the range of values at this radius shown in Figure 2 of IH.

An estimate of the surface density of Draco stars in a field at larger radii is the difference between its value of Σ_{in} in the third block of Table 7 and the lowest value of Σ_{in} , that for the S2 field — which is assumed to be the background. The largest difference, for the SW2 field, is 0.18 ± 0.08 stars arcmin⁻² or 0.0090 ± 0.0039 of the central surface density. We emphasize that this estimate is suspect both because the SW2 field contains a rich cluster of galaxies which contaminates Σ_{in} and because the differences are not statistically significant (see the discussion in Sec. 4.2). The second largest difference is for the E2 field:

0.17 ± 0.08 stars arcmin^{-2} or 0.0083 ± 0.0039 of the central surface density. These values are consistent with the lowest point of the profile shown in Figure 2 of IH (though this is only the lowest point that is above their assumed background). If there are Draco stars in the E2 and W2 fields and not in the N2, S2, and SW2 fields, as suggested by Figures 12(c) and (d) and 13(c) and (d), then the above value for the E2 field is probably an upper limit on their surface density. However, we again emphasize that the evidence for field-to-field fluctuations in the surface density of Draco stars at large radii is weak (see Sec. 4.2).

Several other groups have reported discoveries of stars near or beyond the tidal boundary of the Sextans, Carina, and Sagittarius dSphs.

Gould et al. (1992) identified at least five faint metal-poor dwarf stars, apparently all at a common distance of about 100 kpc, in their CT1 field. This field is about 100 arcmin away from the center of Sextans along the major axis. The properties of these stars are consistent with membership in Sextans and Gould et al. (1992) estimate a surface density, based on these stars, of about 0.01 of the central value for Sextans. The IH value for the major-axis tidal radius of Sextans is 160 ± 50 arcmin, implying that the five stars are within the tidal boundary. The surface density found by Gould et al. (1992) is consistent with the IH profile for Sextans.

Kuhn et al. (1996; hereafter KSH) found evidence for Carina stars in fields up to 2° away from the center of this galaxy along the extension of its major axis. Their approach is similar to our method of searching for field-to-field fluctuations in Σ_{in} , except that it subtracts an estimate of the contribution from non-member objects. They use least squares to estimate the contribution to the CMD of each field from both the CMD of a background field, containing non-member stars and galaxies, and a CMD which is the difference between the CMD of a field centered on Carina and the background CMD, intended to contain only Carina stars. Out of the eight fields along the extension of the major axis and not centered on Carina, seven have surface densities of Carina stars larger than those of the two fields 1° on either side of the center along the extension of the minor axis, which were taken to represent the background. The two nearest of the eight fields have the highest measured contribution from the Carina CMD. The center of the nearest field is slightly within the tidal boundary measured by IH, so the presence of Carina stars in this field is expected and, as KSH note, is consistent with the profile measured by IH. The second nearest field is just outside of the measured tidal boundary of Carina, so the inferred presence of Carina stars there is reminiscent of our evidence for Draco stars in the regions of the E1 and W1 fields outside of the tidal boundary of Draco.

Our values for Σ_{in} for fields about 1° from the center of Draco, shown in the left-most panel of the bottom row of Figure 16, display less scatter than do the values for the

contribution of the Carina CMD to the CMDs of the KSH fields. This is the case even after excluding the two innermost of their fields. The scatter is closer to what we see before removing galaxies (see the left-most panel of the top row of Figure 16). KSH do not remove galaxies from their sample. The uncertainty for the Carina contribution estimated by KSH comes from the scatter of the values from the four quadrants of the field, as do our error bars in the bottom row of Figure 16. Their uncertainties vary more between fields than do ours. This may be due to either or both of the following: the clustering of galaxies on angular scales comparable to the size of the field and the small numbers of objects in each bin of their least-squares fit. Because of the above concerns about galaxies and the variable uncertainties, we think that evidence for Carina stars 1° or more from the center is weaker than KSH claim and is probably no stronger than our evidence for Draco stars in the E2 and W2 fields.

Majewski et al. (2000; hereafter M2K) identified a “substantial extratidal population from Carina” using Washington-band and DDO51-band photometry. With this technique it is possible to distinguish metal-poor giants from the more numerous disk and halo dwarf stars (Geisler 1984) to a degree that depends on photometric accuracy. Based on the size of this population beyond the tidal boundary measured by IH, M2K estimated that Carina loses about 27% of its mass per Gyr. Spectroscopy of three bright giant candidates outside of the tidal boundary confirmed that they have velocities consistent with that of Carina. Notwithstanding this confirmation, Morrison et al. (2000) argued that photometric errors of 0.1 mag, the limit adopted by M2K, cause dwarfs from the Galactic disk and halo to contaminate significantly the population of fainter candidate giants. The photometric and spectroscopic data of M2K demonstrate that there are Carina stars beyond its measured tidal boundary. However, the number of these stars and their distribution in azimuth and radius remain uncertain because of the incomplete areal coverage and variable limiting magnitudes of the M2K fields, and the concerns raised by Morrison et al. (2000).

Since the discovery of the Sagittarius dSph (Ibata et al. 1994), stars associated with this galaxy have been found at ever increasing angular distances from its center. Mateo et al. (1996) and Fahlman et al. (1996) found main-sequence stars of Sagittarius about 10° from the center. Mateo et al. (1996) also found RR Lyrae stars associated with Sagittarius in their field, as did Alard (1996) and Alcock et al. (1997) in fields 8° to 11° from the center on the opposite side. Ibata et al. (1997) detected main-sequence stars in a $22^\circ \times 8^\circ$ region on the side of Sagittarius away from the Galactic plane. They infer a minor axis limiting radius of 4° and a major to minor axis ratio of 3:1, implying a major axis limiting radius of 12° . However, Mateo et al. (1998) detected main-sequence stars over the range of 10° to 34° from the center of Sagittarius. Their measured surface density profile along the major axis has a break at a radius of about 20° . Majewski et al. (1999) report a possible detection of Sagittarius stars

at similar angular distances. Recently, a survey for carbon stars in the Galactic halo (Totten & Irwin 1998; Totten et al. 2000) has found giant carbon stars distributed on a great circle passing through the position of Sagittarius. Ibata et al. (2000a) interpret these stars as a stream of tidal debris extending completely around the orbit of Sagittarius. Ibata et al. (2000b) also argue that halo substructure found in the Sloan Digital Sky Survey (Yanny et al. 2000; Ivezić et al. 2000) is tidal debris from Sagittarius.

The existence of stars beyond the tidal boundary of Sagittarius is established and they are very likely due to tidal stripping. Is this the case for the Galactic dSphs at larger galactocentric distance, for which tides are currently less important? Our study and others, particularly that of Majewski et al. (2000) for Carina, show that several dSphs extend beyond the tidal boundaries measured by IH. However, these stars have not been found to extend to as large a distance along the major axis as for Sagittarius, so alternative explanations remain viable. The most mundane explanation is that these stars are within the tidal boundary of their dSph. This boundary is uncertain because there is no fundamental reason why a King model (King 1966) should correctly describe a dSph at all radii. For example, a dSph could be surrounded by an extended population of bound stars formed when gas in the galaxy was expelled by supernovae and stellar winds.

Convincing evidence for tidal stripping would be the existence of a very extended distribution of stars along some axis, particularly if supported by the presence of a velocity gradient in these stars (Oh et al. 1995; Piatek & Pryor 1995; Johnston et al. 1995). Though this axis must be along the orbit, it is not clear that this must be the major axis of the bound stars since the galaxy might have formed with the major axis not in the orbital plane. Indeed, an alignment between these two could argue for a strong tidal interaction, though this might also be a result of the dSph forming in the vicinity of the Galaxy. Extensions of the work presented in this paper that could provide better evidence for tidal stripping are deeper two-color photometry with good seeing – preferably followed up with radial velocity or proper motion measurements, searches for RR Lyrae variables, and three-color photometry that is able to distinguish metal-poor giants from disk and halo dwarfs.

We thank Janie Fultz for proofreading the text and Mike Irwin for sending us the image of the IH stellar surface density in the vicinity of Draco included in Figure 2. The research of CP and SP was supported by NSF grant AST 96-19510, while that of EWO was partially supported by NSF grant AST 96-19524. This research has made use of the Astronomical Data Center (ADC) at the NASA Goddard Space Flight Center.

REFERENCES

- Alard, C. 1996, *ApJL*, 458, L17
- Alcock, C. et al. 1997, *ApJ*, 474, 217
- Armandroff, T., Massey, P., Silva, D., & Sarajedini, A. 1993, *NOAO Newsletter*, 36, 29
- Baade, W., & Swope, H. H. 1961, *AJ*, 66, 300
- Bellazzini, M., Fusi Pecci, F., & Ferraro, F. R. 1996, *MNRAS*, 278, 947
- Cardelli, J. A., Clayton, G. C., & Mathis, J. S. 1989, *ApJ*, 345, 245
- Carney, B. W., & Seitzer, P. 1986, *AJ*, 92, 23 (CS)
- Ebeling, H., Edge, A. C., Böhringer, H., Allen, S. W., Crawford, C. S., Fabian, A. C., Voges, W., & Huchra, J. P. 1998, *MNRAS*, 301, 881
- Fahlman, G. G., Mandushev, G., Richer, H. B., Thompson, I. B., & Sivaramakrishnan, A. 1996, *ApJL*, 459, L65.
- Geisler, D. 1984, *PASP*, 96, 723
- Gould, A., Guhathakurta, P., Richstone, D., & Flynn, C. 1992, *ApJ*, 388, 345
- Hirashita, H., Kamaya, H., & Takeuchi, T. 1999, *PASJ*, 51, 375
- Hodge, P. W., & Michie, R. W. 1969, *AJ*, 74, 587
- Ibata, R. A., Gilmore, G., & Irwin, M. J. 1994, *Nature*, 370, 194
- Ibata, R., Irwin, M., Lewis, G. F., Stolte, A. 2000b, *ApJL*, submitted (astro-ph/0004255)
- Ibata, R., Lewis, G. F., Irwin, M., Totten, E., & Quinn, T. 2000a, *ApJ*, submitted (astro-ph/0004011)
- Ibata, R. A., Wyse, R. F. G., Gilmore, G., Irwin, M. J., & Suntzeff, N. B. 1997, *AJ*, 113, 634
- Irwin, M. J., & Hatzidimitriou, D. 1995, *MNRAS*, 277, 1354 (IH)
- Ivezić, Z. et al. 2000, *AJ*, 120, 963
- Johnston, K. V., Sigurdsson, S., & Hernquist, L. 1999, *MNRAS*, 302, 771
- Johnston, K. V., Spergel, D. N., & Hernquist, L. 1995, *ApJ*, 451, 598
- Kibblewhite, E. J., Bridgeland, M. T., Bunclark, P. S., & Irwin, M. J. 1984, in *Proc. Astron. Microdensitometry Conf. NASA-2317*, ed. D. Klingle-Smith (Washington, DC: NASA), 277
- King, I. R. 1966, *AJ*, 71, 64

- Klessen, R. S., & Kroupa, P. 1998, *ApJ*, 498, 143
- Kuhn, J. R., & Miller, R. H. 1989, *ApJ*, 341, L41
- Kuhn, J. R., Smith, H. A., & Hawley, S. L. 1996, *ApJL*, 469, L93 (KSH)
- Landolt, A. U. 1983, *AJ*, 88, 439
- Landolt, A. U. 1992, *AJ*, 104, 340
- Lin, D. N. C., & Murray, S. D. 1998, in *Dwarf Galaxies and Cosmology*, ed. T. X. Thuan, C. Balkowski, V. Cayatte, & J. T. T. Van (Paris: Editions Frontieres), 433
- Majewski, S. R., Ostheimer, J. C., Patterson, R., Kunkel, W. E., Johnston, K. V., & Geisler, D. 2000, *AJ*, 119, 760 (M2K)
- Majewski, S. R., Siegel, M. H., Kunkel, W. E., Reid, I. N., Johnston, K. V., Thompson, I. B., Landolt, A. U., & Palma, C. 1999, *AJ*, 118, 1709
- Mateo, M., Mirabal, N., Udalski, A., Szymański, M., Kałużny, J., Kubiak, M., Krzemiński, W., and Stanek, K. Z. 1996, *ApJL*, 458, L13
- Mateo, M., Olszewski, E. W., & Morrison, H. L. 1998, *ApJ*, 508, L55
- McClure, R. D., VandenBerg, D. A., Bell, R. A., Hesser, J. E., and Stetson, P. B. 1987, *AJ*, 93, 1144
- Monet, D. et al. 1998, *USNO-A V2.0*, A Catalog of Astrometric Standards (Washington, DC: US Naval Observatory)
- Moore, B. 1996, *ApJL*, 461, L13
- Morrison, H. L., Olszewski, E. W., Mateo, M., Norris, J. E., Harding, P., Dohm-Palmer, R. C., & Freeman, K. C. 2000, *AJ*, submitted
- Oh, K. S., Lin, D. N. C., & Aarseth, S. J. 1995, *ApJ*, 442, 142
- Olszewski, E. W. 1998, in *ASP Conf. Ser. 136*, *Galactic Halos: A UC Santa Cruz Workshop*, ed. D. Zaritsky (San Francisco: ASP), 70
- Piatek, S., & Pryor, C. 1995, *AJ*, 109, 1071
- Piatek, S., Pryor, C., Olszewski, E. W., & Armandroff, T. E., 2000, in preparation
- Pryor, C. 1994, in *Dwarf Galaxies*, ed. G. Meylan & P. Prugniel (Garching: ESO), 323
- Pryor, C. 1996, in *ASP Conf. Ser. Vol. 92*, *Formation of the Galactic Halo...Inside and Out*, ed. H. L. Morrison & A. Sarajedini (San Francisco: ASP), 424
- Puche, D., & Westpfahl, D. 1994, in *Dwarf Galaxies*, ed. G. Meylan & P. Prugniel (Garching: ESO), 273
- Reid, N., & Majewski, S. R. 1993, *ApJ*, 409, 635

- Schlegel, D. J., Finkbeiner, D. P., & Davis, M. 1998, *ApJ*, 500, 525
- Stetson, P.B. 1987, *PASP*, 99, 191
- Stetson, P.B. 1992, in *ASP Conf. Ser. Vol. 25, Astronomical Data Analysis Software and Systems*, ed. D. M. Worrall, C. Biemesderfer, & J. Barnes (San Francisco: ASP), 297
- Stetson, P.B. 1994, *PASP*, 106, 250
- Stetson, P. B., VandenBerg, D. A., & McClure, R. D. 1985, *PASP*, 97, 908 (SVM)
- Totten, E. J., & Irwin, M. J. 1998, *MNRAS*, 294, 1
- Totten, E. J., Irwin, M. J., & Whitelock, P. 2000, *MNRAS*, 314, 630
- Webbink, R. F. 1985, in *IAU Symp. 113, Dynamics of Star Clusters*, ed. J. Goodman & P. Hut (Dordrecht: Reidel), 541
- Yanny, B., et al. 2000, *ApJ*, 540, 825

Figure Captions

Fig. 1. The locations of our fields superimposed on the Digitized Sky Survey image centered on Draco. The ellipse represents the measured tidal boundary of Draco.

Fig. 2. The locations of our fields superimposed on a map of the surface density of stars and galaxies derived by Irwin & Hatzidimitriou (1995).

Fig. 3. A comparison of the V-band magnitudes derived by Stetson et al. (1985) (V_{SVM}) and the authors (V_{us}) for the 95 objects common to both studies. All of the objects are in our C0 field.

Fig. 4. A comparison of the V-band magnitudes derived by Carney & Seitzer (1986; CS) (V_{CS}) and the authors (V_{us}). CS measured two independent magnitudes for some objects and these appear twice among the 1382 points in the plot. A point marked with a slanted cross corresponds to a confirmed RR Lyrae star.

Fig. 5. (a) A comparison of the R-band magnitudes for the 190 objects common to the E1 and C0 fields. (b) The same as Fig. 5a for the V band.

Fig. 6. (a) A comparison of the R-band magnitudes for the 54 objects common to the E1 and SE1 fields. (b) The same as Fig. 6a for the V band.

Fig. 7. (a) A comparison of the R-band magnitudes for the 83 objects common to the S2 and SW2 fields. (b) The same as Fig. 7a for the V band.

Fig. 8. R-band magnitude vs. SHARP for all of the objects in the C0 field. The lines represent the SHARP limits that we have adopted in this study.

Fig. 9. Color-magnitude diagrams for our 9 fields. The R and V magnitudes are from Tables 4(a) through 4(i). Only objects with CHI values less than 5 and SHARP values within the limits shown in Fig. 8 are shown on these diagrams. The principal sequences of Draco are apparent in the diagrams for the C0, E1, and W1 fields.

Fig. 10. The location of our fields superimposed on the map of $E(B - V)$ derived from dust infrared emission by Schlegel et al. (1998). Lighter shades correspond to larger reddening.

Fig. 11. Color-magnitude diagram for the C0 field. The R and V magnitudes are not corrected for reddening and extinction. The solid contour encloses our adopted region containing stars likely to belong to Draco. Its width is approximately determined by the color uncertainty at each magnitude. The few points marked with a cross correspond to some confirmed RR Lyrae stars.

Fig. 12. (a) Color-magnitude diagram for the combination of those sections of the E1, SE1, and W1 fields outside of the measured tidal boundary of Draco. (b) Color-magnitude diagram for the C0 field. This diagram serves as a reference. (c) The same as (a), with the addition of objects from the E2 and W2 fields. (d) The same as (a), with the addition of objects from the N2, S2, and SW2 fields.

Fig. 13. Gray-scale Hess diagrams for the CMDs in Figure 12. Darker shades correspond to a larger density of points. The contour in (a), (c), and (d) is an isopleth from (b) that outlines the expected principal sequences of Draco. (a) The Hess diagram corresponding to Figure 12(a). (b) The same as (a) for the CMD in Figure 12(b). (c) The same as (a) for the CMD in Figure 12(c). (d) The same as (a) for the CMD in Figure 12(d).

Fig. 14. (a) Color-magnitude diagram for those quadrants of fields with higher than average values of Σ_{in} . (b) Color-magnitude diagram for those quadrants of fields with higher than average values of $\Sigma_{\text{in}}/\Sigma_{\text{out}}$. (c) Gray-scale Hess diagram for the CMD in (a). Darker shades correspond to a larger density of points. The contour is an isopleth from Figure 12(b) that outlines the expected principal sequences of Draco. (d) The same as (c) for the CMD in (b).

Fig. 15. (a) The fractional rms scatter of Σ_{in} around its mean as a function of limiting magnitude (solid squares) for the fields N2, E2, S2, SW2, and W2, and those sections of the SE1 and W1 fields outside of the measured tidal boundary of Draco. Σ_{in} includes objects regardless of their CHI and SHARP values. The open squares represent the scatter expected from Poisson noise. (b) The same as (a) for Σ_{out} . (c) The same as (a) for $\Sigma_{\text{in}}/\Sigma_{\text{out}}$. (d) The same as (a) for Σ_{in} including only objects with CHI values less than 5.0 and SHARP values within the limits shown in Fig. 8. (e) The same as (d) for Σ_{out} . (f) The same as (d) for $\Sigma_{\text{in}}/\Sigma_{\text{out}}$.

Fig. 16. The values of Σ_{in} , Σ_{out} , and $\Sigma_{\text{in}}/\Sigma_{\text{out}}$ to a limiting magnitude $R = 22.6$ for the fields SE1, W1* (the section of W1 outside of the measured tidal boundary of Draco), N2, E2, S2, SW2, and W2. The top panels show values calculated including objects regardless of their CHI and SHARP values. The error bars are σ_{int} , the Poisson noise. The middle panels are the same as the top panels for values calculated including objects with CHI values less than 5.0 and SHARP values within the limits shown in Fig. 8. The bottom panels are the same as the middle panels, but with the error bars given σ_{ext} — the rms scatter around the mean value for the four quadrants of the field. No point is plotted for W1* since σ_{ext} cannot be determined for this section of the W1 field.

TABLE 1. Information about Draco's fields

| Field | Date dd/mm/yy | R.A. (2000.0) | Dec. (2000.0) | l degrees | b degrees | T_{exp} | | V s | R s | V pix |
|---------|------------------|------------------|------------------|--------------|--------------|-----------|--------|--------|--------|----------------|
| | | | | | | | | | | |
| C0 | 19/07/91 | 17:20:07.19 | 57:55:35.80 | 86.3824 | 34.7324 | 3×1800 | 3×1800 | | | 2.22 ± 0.2 |
| E1 | 18/05/93 | 17:22:55.43 | 57:53:05.66 | 86.3066 | 34.3629 | 4×1500 | 3×1500 | | | 2.35 ± 0.5 |
| E1(tie) | 10/06/94 | 17:21:28.45 | 57:54:34.20 | 86.3488 | 34.5539 | 1×200 | 1×200 | | | ... |
| SE1 | 12/06/94 | 17:22:56.61 | 57:30:14.91 | 85.8457 | 34.3786 | 4×1500 | 3×1500 | | | 2.64 ± 0.0 |
| W1 | 10/06/94 | 17:17:06.49 | 57:54:30.09 | 86.3929 | 35.1327 | 4×1500 | 3×1500 | | | 2.58 ± 0.0 |
| N2 | 09/06/94 | 17:20:12.95 | 59:00:14.59 | 87.6888 | 34.6470 | 4×1500 | 3×1500 | | | 2.66 ± 0.1 |
| E2 | 12/06/94 | 17:28:03.24 | 58:16:00.38 | 86.7318 | 33.6690 | 4×1500 | 3×1500 | | | 2.46 ± 0.1 |
| S2 | 09/06/94 | 17:20:03.97 | 56:45:54.52 | 84.9711 | 34.8030 | 4×1500 | 3×1500 | | | 2.45 ± 0.1 |
| SW2 | 13/06/94 | 17:17:17.00 | 56:45:23.18 | 84.9851 | 35.1842 | 4×1500 | 3×1500 | | | 2.53 ± 0.0 |
| W2 | 11/06/94 | 17:10:19.57 | 57:53:56.84 | 86.4764 | 36.0310 | 4×1500 | 4×1500 | | | 2.59 ± 0.0 |

TABLE 2. Photometric Coefficients for 1994 Run

| Night | a | d | b | e | c | f |
|-------|-------|-------|-------|---------|-------|-------|
| 1 | 4.415 | 4.271 | 0.004 | −0.0138 | 0.139 | 0.134 |
| 2 | 4.438 | 4.295 | 0.004 | −0.0138 | 0.139 | 0.134 |
| 3 | 4.486 | 4.342 | 0.004 | −0.0138 | 0.139 | 0.134 |
| 4 | 4.450 | 4.308 | 0.004 | −0.0138 | 0.139 | 0.134 |
| 5 | 4.446 | 4.300 | 0.004 | −0.0138 | 0.139 | 0.134 |

TABLE 3.
Average Airmasses

| Field | X (V) | X' (R) |
|-------|-------|--------|
| C0 | 1.747 | 1.787 |
| E1 | ... | ... |
| SE1 | 1.254 | 1.232 |
| W1 | 1.147 | 1.311 |
| N2 | 1.153 | 1.294 |
| E2 | 1.126 | 1.127 |
| S2 | 1.128 | 1.250 |
| SW2 | 1.149 | 1.108 |
| W2 | 1.147 | 1.206 |

TABLE 4. (a) R and V Photometry of Draco: C0 field.^a

| Star | X (pix) | Y (pix) | RA (2000.0) | | | Dec (2000.0) | | | R | σ_R | V | σ_V | CHI | SHARP |
|------|----------|----------|-------------|----|-------|--------------|----|-------|---------|------------|---------|------------|---------|--------|
| 1 | 682.848 | 925.791 | 17 | 20 | 13.29 | 57 | 58 | 29.07 | 13.0732 | 0.0440 | 15.4430 | 0.2020 | 8.6150 | 1.4900 |
| 2 | 682.761 | 931.340 | 17 | 20 | 12.81 | 57 | 58 | 29.21 | 13.1683 | 0.0400 | 14.8302 | 0.3420 | 13.2250 | 0.8175 |
| 3 | 935.689 | 714.228 | 17 | 20 | 31.11 | 57 | 55 | 31.72 | 13.2900 | 0.0190 | 13.6947 | 0.0820 | 2.6500 | 0.4470 |
| 4 | 1608.817 | 1437.454 | 17 | 19 | 27.45 | 57 | 47 | 58.23 | 13.3933 | 0.0460 | 13.6090 | 0.0330 | 2.2900 | 0.9055 |
| 5 | 1270.808 | 1004.486 | 17 | 20 | 05.39 | 57 | 51 | 45.21 | 13.4068 | 0.0590 | 13.2914 | 0.5900 | 11.0250 | 0.8665 |

^aThe complete version of this table is in the electronic edition of the Journal. The printed edition contains only a sample.

TABLE 5. Completeness Percentages

| Field | R | | | | | |
|-------|----------------|----------------|----------------|----------------|----------------|----------------|
| | 22.1 | 22.6 | 23.1 | 23.35 | 23.6 | 23.85 |
| C0 | 92.7 ± 1.1 | 76.5 ± 1.7 | 35.3 ± 2.0 | 21.0 ± 1.7 | 11.8 ± 1.3 | 7.7 ± 1.1 |
| E1 | 96.8 ± 0.7 | 95.0 ± 0.9 | 84.7 ± 1.5 | 70.8 ± 1.9 | 54.8 ± 2.0 | 38.7 ± 2.0 |
| SE1 | 96.8 ± 0.7 | 95.5 ± 0.8 | 80.8 ± 1.6 | 57.5 ± 2.0 | 42.7 ± 2.0 | 27.0 ± 1.8 |
| W1 | 97.0 ± 0.7 | 96.0 ± 0.8 | 78.7 ± 1.7 | 58.3 ± 2.0 | 32.2 ± 1.9 | 17.7 ± 1.6 |
| N2 | 98.2 ± 0.5 | 95.0 ± 0.9 | 91.0 ± 1.2 | 76.0 ± 1.7 | 51.2 ± 2.0 | 29.3 ± 1.9 |
| E2 | 97.7 ± 0.6 | 95.8 ± 0.8 | 89.0 ± 1.3 | 79.7 ± 1.6 | 49.2 ± 2.0 | 27.5 ± 1.8 |
| S2 | 98.5 ± 0.5 | 96.7 ± 0.7 | 93.8 ± 1.0 | 83.2 ± 1.5 | 60.0 ± 2.0 | 34.2 ± 1.9 |
| SW2 | 96.2 ± 0.8 | 94.2 ± 1.0 | 85.5 ± 1.4 | 63.0 ± 2.0 | 35.7 ± 2.0 | 18.2 ± 1.6 |
| W2 | 97.7 ± 0.6 | 95.7 ± 0.8 | 78.8 ± 1.7 | 46.8 ± 2.0 | 25.2 ± 1.8 | 14.3 ± 1.4 |

TABLE 6. Reddening, V and R extinctions,
and color of the blue edge

| Field | $E(B - V)$ (mag) | A_V (mag) | A_R (mag) | Color ^a (mag) |
|-------|---------------------|----------------|----------------|-----------------------------|
| C0 | 0.029 | 0.095 | 0.076 | 0.240 |
| E1 | 0.029 | 0.097 | 0.078 | 0.297 |
| SE1 | 0.027 | 0.090 | 0.073 | 0.326 |
| W1 | 0.028 | 0.093 | 0.075 | 0.311 |
| N2 | 0.026 | 0.087 | 0.070 | 0.307 |
| E2 | 0.037 | 0.122 | 0.098 | 0.295 |
| S2 | 0.026 | 0.086 | 0.069 | 0.302 |
| SW2 | 0.024 | 0.081 | 0.065 | 0.289 |
| W2 | 0.020 | 0.067 | 0.054 | 0.340 |

^aThis is the dereddened color. We discuss the variation in these values in the text.

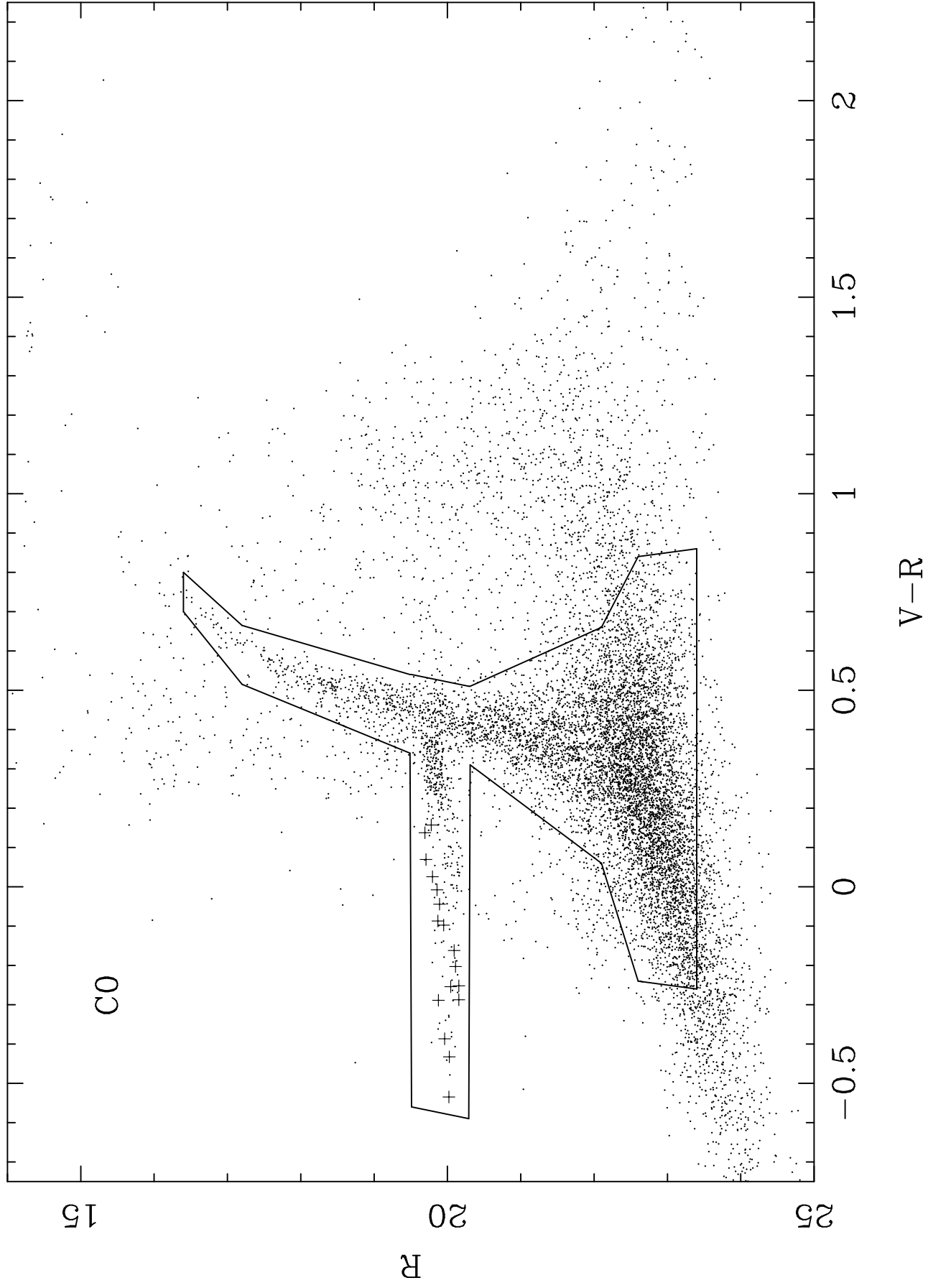
TABLE 7. Results

| Quantity | C0 | E1 | SE1 | W1 | Field N2 | E2 | S2 | SW2 | W2 |
|--|-------------|-------------|-------------|-------------|-------------|-------------|-------------|-------------|-------------|
| Area | 457.34 | 537.71 | 536.00 | 536.33 | 536.69 | 534.74 | 535.64 | 536.14 | 535.72 |
| No Cuts | | | | | | | | | |
| Σ_{in} | 10.465 | 3.336 | 2.198 | 3.282 | 2.542 | 2.601 | 2.530 | 2.913 | 2.550 |
| σ_{int} | ± 0.151 | ± 0.079 | ± 0.064 | ± 0.078 | ± 0.069 | ± 0.070 | ± 0.069 | ± 0.074 | ± 0.069 |
| σ_{ext} | ± 1.304 | ± 0.519 | ± 0.065 | ± 0.211 | ± 0.043 | ± 0.129 | ± 0.154 | ± 0.220 | ± 0.189 |
| Σ_{out} | 6.101 | 4.515 | 4.187 | 4.706 | 4.422 | 4.329 | 4.807 | 5.105 | 4.387 |
| σ_{int} | ± 0.115 | ± 0.092 | ± 0.088 | ± 0.094 | ± 0.091 | ± 0.090 | ± 0.095 | ± 0.098 | ± 0.090 |
| σ_{ext} | ± 0.160 | ± 0.182 | ± 0.153 | ± 0.151 | ± 0.155 | ± 0.148 | ± 0.128 | ± 0.290 | ± 0.208 |
| $\Sigma_{\text{in}}/\Sigma_{\text{out}}$ | 1.715 | 0.739 | 0.525 | 0.697 | 0.575 | 0.601 | 0.526 | 0.571 | 0.581 |
| σ_{int} | ± 0.025 | ± 0.017 | ± 0.015 | ± 0.017 | ± 0.016 | ± 0.016 | ± 0.014 | ± 0.014 | ± 0.016 |
| σ_{ext} | ± 0.219 | ± 0.137 | ± 0.026 | ± 0.052 | ± 0.020 | ± 0.035 | ± 0.031 | ± 0.022 | ± 0.034 |
| With Cuts | | | | | | | | | |
| Σ_{in} | 9.483 | 2.959 | 1.552 | 2.357 | 1.556 | 1.677 | 1.512 | 1.692 | 1.648 |
| σ_{int} | ± 0.144 | ± 0.074 | ± 0.054 | ± 0.066 | ± 0.054 | ± 0.056 | ± 0.053 | ± 0.056 | ± 0.055 |
| σ_{ext} | ± 1.217 | ± 0.546 | ± 0.056 | ± 0.204 | ± 0.046 | ± 0.052 | ± 0.043 | ± 0.057 | ± 0.089 |
| Σ_{out} | 3.700 | 3.904 | 3.103 | 3.205 | 2.983 | 3.119 | 3.174 | 3.279 | 2.880 |
| σ_{int} | ± 0.090 | ± 0.085 | ± 0.076 | ± 0.077 | ± 0.075 | ± 0.076 | ± 0.077 | ± 0.078 | ± 0.073 |
| σ_{ext} | ± 0.142 | ± 0.173 | ± 0.137 | ± 0.112 | ± 0.095 | ± 0.073 | ± 0.145 | ± 0.071 | ± 0.040 |
| $\Sigma_{\text{in}}/\Sigma_{\text{out}}$ | 2.563 | 0.758 | 0.500 | 0.735 | 0.522 | 0.538 | 0.476 | 0.516 | 0.572 |
| σ_{int} | ± 0.039 | ± 0.019 | ± 0.017 | ± 0.021 | ± 0.018 | ± 0.018 | ± 0.017 | ± 0.017 | ± 0.019 |
| σ_{ext} | ± 0.257 | ± 0.167 | ± 0.036 | ± 0.078 | ± 0.009 | ± 0.024 | ± 0.010 | ± 0.013 | ± 0.025 |

^aIn the calculation of the mean of Σ_{in} and $\Sigma_{\text{in}}/\Sigma_{\text{out}}$, we excluded the C0, E1, and W1 fields. In the calculation of σ_{ext} , we excluded the C0 and E1 fields.

This figure "piatek.fig10.jpg" is available in "jpg" format from:

<http://arxiv.org/ps/astro-ph/0011006v1>



This figure "piatek.fig12.gif" is available in "gif" format from:

<http://arxiv.org/ps/astro-ph/0011006v1>

This figure "piatek.fig13.jpg" is available in "jpg" format from:

<http://arxiv.org/ps/astro-ph/0011006v1>

This figure "piatek.fig14.jpg" is available in "jpg" format from:

<http://arxiv.org/ps/astro-ph/0011006v1>

